AFOSR-TR-95

REPORT DOCUMENTATION PAGE

0628

1. AGENCY USE ONLY (Leave blank)	2. REPORT DATE 951506	3. REPORT Final Report 941504 to 951404

4. TITLE AND SUBTITLE Nano-Structures via Diffusion Limited Crystallization from Solution Precursors: Synthesis and Properties	5. FUNDING NUMBERS AFOSR F49620-94-1-0229 2306/BS

6. AUTHOR(S) Fred F. Lange	

7. PERFORMING ORGANIZATION NAME(S) AND ADDRESS(ES) Materials Department College of Engineering University of California Santa Barbara, CA 93106-5050	8. PERFORMING ORGANIZATION REPORT NUMBER

DTIC ELECTED S OCT 1 2 1995 G

9. SPONSORING/MONITORING AGENCY NAME(S) AND ADDRESS(ES) DR. ALEXANDER PECHENIK AFOSR/NA 110 DUNCAN AVENUE SUITE B115 BOLLING AFB DC 20332-0001	10. SPONSORING/MONITORING AGENCY REPORT NUMBER F49620- 94-1-0229

11. SUPPLEMENTARY NOTES

13. ABSTRACT (Maximum 200 words)

This program has emphasized two topics: 1) the crystallization of metastable, solid-solution structures, their partitioning into equilibrium structures and compositions, and the role of the metastable phase and its partitioning on forming unique, nanometer microstructures important to the mechanics of structural ceramics and their composites, and 2) the formation of single crystal thin films via spin coating single crystal substrates with solution precursors. Results for the first topic are new, namely, the discovery that diffusion limited crystallization concepts used in rapid solidification directly applies to precursors that crystallize at low temperatures during heating. This discovery is significant because solid-solutions can be greatly extended relative to high temperature synthesis and processing routes where equilibrium conditions are rapidly achieved and solid-solutions can be severely limited. Extension of solid-solution fields (and thus defect chemistries) in compositional space is important to synthesize new materials with optical and electronic properties controlled by defect chemistry and/or metastable compositions. Results for the second topic have shown that single crystal thin films can be formed on single crystal substrates with spin-on liquid precursors despite large differences in lattice parameters and/or crystal structures. Several mechanisms have been identified for the growth of single crystal thin films which are very different to the well know vapor phase epitaxy mechanisms. The significance of the second topic is that single crystal (or poly-variant single crystal) thin films of nearly any inorganic material can be produced on any non-reactive (thermodynamically or kinetically) single crystal substrate, despite crystal structure differences between the film and substrate materials. Processing of multi-layer and/or embedded strip line architectures are possible using liquid precursor spin-on techniques for new device technologies.

14. SUBJECT TERMS NANO-STRUCTURES, DIFFUSION, CRYSTALLIZATION, SOLUTION PRESURSORS		15. NUMBER OF PAGES 95
		16. PRICE CODE

17. SECURITY CLASSIFICATION OF REPORT Unclassified	18. SECURITY CLASSIFICATION OF THIS PAGE Unclassified	19. SECURITY CLASSIFICATION OF ABSTRACT Unclassified	20. LIMITATION OF ABSTRACT

Nano-Structures via Diffusion Limited Crystallization from Solution Precursors: Synthesis and Properties

Contract AFOSR F49620-94-1-0229

Final Report

period: April 15, 1994-April 14, 1995

September, 1995

From

Materials Department
College of Engineering
University of California
Santa Barbara, CA 93106

Accesion For	
NTIS CRA&I	☒
DTIC TAB	☐
Unannounced	☐
Justification	

By	
Distribution /	
Availability Codes	

Dist	Avail and / or Special
A-1	

Principal Investigator: Fred F. Lange

1. Background

This program has emphasized two topics: 1) the crystallization of metastable, solid-solution structures, their partitioning into equilibrium structures and compositions, and the role of the metastable phase and its partitioning on forming unique, nanometer microstructures important to the mechanics of structural ceramics and their composites, and 2) the formation of single crystal thin films via spin coating single crystal substrates with solution precursors. Results for the first topic are new, namely, the discovery that diffusion limited crystallization concepts used in rapid solidification directly applies to precursors that crystallize at low temperatures during heating. This discovery is significant because solid-solutions can be greatly extended relative to high temperature synthesis and processing routes where equilibrium conditions are rapidly achieved and solid-solutions can be severely limited. Extension of solid-solution fields (and thus defect chemistries) in compositional space is important to synthesize new materials with optical and electronic properties controlled by defect chemistry and/or metastable compositions. Results for the second topic have shown that single crystal thin films can be formed on single crystal substrates with spin-on liquid precursors despite large differences in lattice parameters and/or crystal structures. Several mechanisms have been identified for the growth of single crystal thin films which are very different to the well know vapor phase epitaxy mechanisms. The significance of the second topic is that single crystal (or poly-variant single crystal) thin films of nearly any inorganic material can be produced on any non-reactive (thermodynamically or kinetically) single crystal substrate, despite crystal structure differences between the film and substrate materials. Processing of multi-layer and/or embedded strip line architectures are possible using liquid precursor spin-on techniques for new device technologies.

2. Summary of Research

2.1 Single Crystal Thin Films via Solution Precursors, F.F. Lange

Technical Report No. 1 (and Final Report)

Abstract: Solutions containing different precursor molecules can be used to coat a single crystal substrate and synthesize a multi-element, inorganic material. At low temperatures the precursor film decomposes to a partially dense, polycrystalline film. This review will describe the different phenomena responsible for converting the polycrystalline film to a single crystal film at higher temperatures. These phenomena include abnormal grain growth and a morphological instability responsible for the epitaxy of materials of unlike structure, e.g., ZrO_2 on basal plane sapphire; the reaction of the coating with the substrate, e.g., to epitaxy rare-earth hexa-aluminates ($NdAl_{11}O_{18}$) on basal plane sapphire; grain growth that initiates on the substrate when lattice mismatch is small, e.g., cubic-ZrO_2 on cubic-ZrO_2 substrates and $PbTiO_3$ on $SrTiO_3$.

2.2 Microstructural Instability in Single Crystal Thin Films, A. Seifert, A. Vojta, J.S. Speck, and F.F. Lange

Technical Report No. 2 (and Final Report)

Abstract: Epitaxial $PbTiO_3$ thin films were produced from a mixed Pb-Ti-double-alkoxide precursor by spin-coating onto single crystal (001) $SrTiO_3$ substrates. Heat-treatment at 800°C produces a dense and continuous, epitaxial lead titanate film through an intermediate Pb-Ti-fluorite structure. A microstructural instability occurred when very thin single crystal films were fabricated; this instability caused the films to become discontinuous. Scanning electron microscopy and atomic force microscopy observations show that single crystal films with a thickness less than ~80 nm developed holes that expose the substrate; thinner films broke up into isolated, single crystal islands. The walls of the holes were found to be (111) perovskite planes. A free energy function, which considered the anisotropic surface energies of different planes, was developed to describe the microstructural changes in the film and to understand the instability phenomenon. The function predicted that pre-existing holes greater than a critical size are necessary to initiate hole growth and it predicted the observed morphological changes in the current system. Morphological stability diagrams that explain the stability fields for different film configurations, *i.e.*, either completely covered, with holes, or single crystal islands, can be calculated for any film/substrate system.

2.3 "Infiltration of Porous Alumina Bodies with Solution Precursors: Strengthening via Compositional Grading, Grain Size Control and Transformation Toughening"

Paul Honeyman-Colvin* and Fred F. Lange

Technical Report No. 3 (and Final Report)

Abstract: Alumina powder compacts, partially densified with a low temperature heat treatment and then cut into bars, were infiltrated with liquid precursors that decomposed to either mullite ($3Al_2O_3 \cdot 2SiO_2$), fully stabilized zirconia (cubic-$Zr(8Y)O_2$), or partially stabilized zirconia (tetragonal-$Zr(4Y)O_2$). The specimens were repeatedly infiltrated and pyrolyzed to achieve a higher concentration of the precursor near the surface. The infiltrated bodies were then densified at 1500 °C/2 h. Residual stresses developed during cooling from the densification because of the higher concentration of the second phase near the surface. At least 10 bars of each two-phase material were fractured in 4-point bending to determine the effect of the second phase on strength. The alumina bars without a second phase had a larger grain size ($\approx 7\ \mu m$) and a mean strength of 253 MPa. Both intruded phases significantly reduced the grain size to $\approx 1\mu m$. Despite their higher concentration near the surface and apparent surface tensile stress, both of the $Zr(Y)O_2$ phases increased the mean strength to 413 MPa (c-$Zr(8Y)O_2$) and 582 MPa (t-$Zr(4Y)O_2$-an apparent toughening agent). The mullite second phase produced a high mean strength of 588 MPa, due apparently, to its concentration gradient and the apparent, compressive surface stress.

2.4 "Pyrolysis of Pb(Zr0.5Ti0.5)O3 Precursors: Avoiding Pb Partitioning During Pyrolysis," A.D. Polli and F.F. Lange

Technical Report No. 4 (and Final Report)

Abstract: Three different chemical precursor routes were investigated to synthesize $Pb(Zr_{0.5}Ti_{0.5})O_3$: mixing hexanoates, acetate complexing of alkoxides and the synthesis of a mixed alkoxide by the reaction of Ti- and Zr-alkoxide with Pb-acetate. For each, elemental Pb and PbO were the first crystalline phase observed during pyrolysis conditions that involved rapid heating (e.g. to 400 °C). The formation of Pb (and PbO) could be avoided by first heat treating hydrolyzed, mixed alkoxide precursor powders at 300°C for 1hour. This treatment was not effective for the two other precursors. It is concluded that both the carbonaceous content of the precursor (lowest for the hydrolyzed, mixed alkoxides) and the rate of hydrocarbon release during pyrolysis is critical to avoid the formation of elemental Pb during pyrolysis.

Nano-Structures via Diffusion Limited Crystallization from Solution Precursors: Synthesis and Properties

Contract AFOSR F49620-94-1-0229

Final Report

and Technical Report No. 1

period: April 15, 1994-April 14, 1995

SINGLE CRYSTAL THIN FILMS VIA SOLUTION PRECURSORS

F.F. Lange

Materials Department
College of Engineering
University of California, Santa Barbara
Santa Barbara, CA 93106

SINGLE CRYSTAL THIN FILMS
VIA SOLUTION PRECURSOR PROCESSING

FRED F. LANGE

Materials Department

College of Engineering

University of California at Santa Barbara

Santa Barbara, CA 93106

Abstract. Solutions containing different precursor molecules can be used to coat a single crystal substrate and synthesize a multi-element, inorganic material. At low temperatures the precursor film decomposes to a partially dense, polycrystalline film. This review will describe the different phenomena responsible for converting the polycrystalline film to a single crystal film at higher temperatures. These phenomena include abnormal grain growth and a morphological instability responsible for the epitaxy of materials of unlike structure, e.g., ZrO_2 on basal plane sapphire; the reaction of the coating with the substrate, e.g., to epitaxy rare-earth hexa-aluminates ($NdAl_{11}O_{18}$) on basal plane sapphire; grain growth that initiates on the substrate when lattice mismatch is small, e.g., cubic-ZrO_2 on cubic-ZrO_2 substrates and $PbTiO_3$ on $SrTiO_3$.

1   Introduction

As reviewed elsewhere, [1] a variety of solution chemistries (soluble metallorganics, salts, gel forming reactants, etc.) exist to synthesize multi-element oxides. These solutions can be used to coat substrates via either spin-coating or dip-coating. Excess solvent removed during coating forms a solid (or gel) precursor film that pyrolyzes to the desired compound during a low temperature heat treatment (usually < 500 °C). Because pyrolysis occurs at very low temperatures relative to the compound's melting temperature, the free energy change for crystallization, ΔG_c, is large, and the critical nucleus size required for spontaneous crystallization is small. Thus, the crystallization of a connective (partially sintered) network of

nano-crystallites (< 2 nm) is commonly observed: crystallization typically occurs at temperatures were long-range diffusion is kinetically limited and thus metastable phases (extended solid-solutions and non-equilibrium structures) can crystallize.[2,3]

The film decreases its volume during drying, pyrolysis and densification; 'mud' cracks can arise since shrinkage is biaxially constrained by the substrate. It can be shown [1] that cracking is completely avoided if the thickness of the film is less than a critical value (usually ≤ 100 nm). Thus, processors have learned to form thicker films by building up the film thickness with a number of coating and pyrolysis steps, each of which avoids cracking.

When the substrate is a single crystal, epitaxial grain growth, i.e., the preferential growth of grains with specific orientations, can not be avoided due to anisotropic interfacial energies [4] despite lattice mismatch, lack of similarities between film and substrate structures or film-substrate reactivity. A number of different phenomena responsible for converting the polycrystalline film into a single crystal have been uncovered and reviewed below.

2 Epitaxy via Abnormal Grain Growth and Morphological Instability

The most general case for epitaxy occurs when the film and substrate do not have the same structure. As recently reviewed by Thompson et al. [4,5] grain growth in thin films may not be strongly influenced by either the substrate or the film's surface until the grains grow large enough to form a columnar microstructure. Once the grains are larger than the film thickness, grains with specific orientations will undergo abnormal grain growth because of their lower surface and/or interfacial energies. Thus, polycrystalline films with columnar microstructures are expected undergo abnormal grain growth and develop at least one preferred orientation due to anisotropic surface and/or interfacial energies even when the substrate is amorphous.

For single crystal substrates, the in-plane orientation of abnormal grains is generally dictated by the substrate, viz., special grain orientations, crystallographically related to the substrate, have lower interfacial energies. That is, one out-of-plane orientation many have different crystallographic related in-plane variants with identical interfacial energies. Films of this nature generally undergo the morphological instability phenomena described below before abnormal grains grow and impinge upon one another.

The morphological instability that occurs in thin, polycrystalline films causes the film to uncover the substrate during grain growth, and eventually, produce a microstructure where every grain appears as an island. Srolovitz and Safrin [6] were the first an understand this

instability phenomena. They calculated the growth of pin holes in thin films and suggested that a pin hole in a polycrystalline thin film could result from the deepening of the grain boundary groove at a three grain junction during grain growth. Miller et al. [7] reported experimental evidence for Zr(Y)O$_2$ thin films on unoriented sapphire substrates, showing that, indeed, small holes develop at three grain junctions when larger grains consume smaller grains by either grain boundary motion or suface diffusion and then 'spherodize' to minimize their surface energy. They also presented a thermodynamic analysis showing that the break-up process lowers the free energy of the system when the grain size to film thickness ratio exceeds a critical value, $(D/t)_c$, which depends on the dihedral angle (a measure of the grain boundary to surface energy ratio) and the solid-state 'wetting angle' of grains with the substrate.
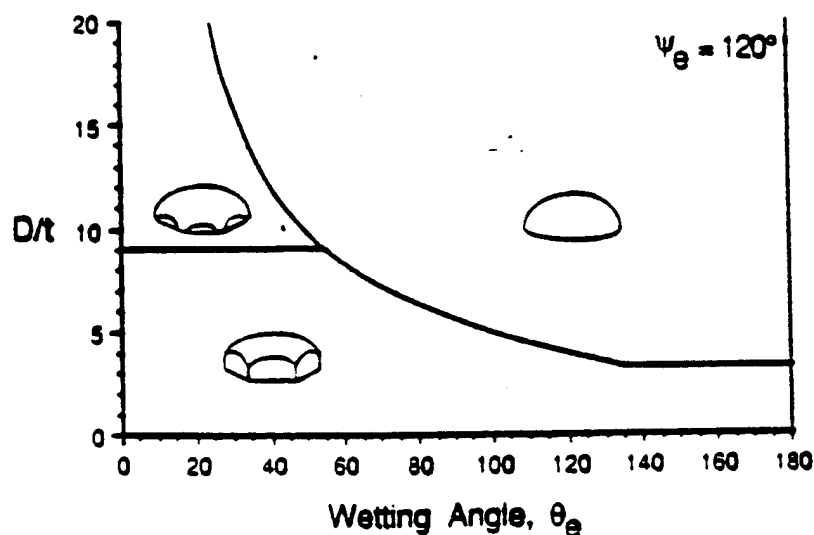

Figure 1 Equilibrium configuration diagram for polycrystalline thin films with columnar microstructures. Boundaries represent the conditions (D/t and solid-state wetting angle) where different configurations have the same free energy. [7] (D = average grain size, t = film thickness)

Miller et al. [7] summarized their thermodynamic calculations with an equilibrium, configurational diagram shown in Fig. 1, where the ratio D/t is plotted as a function of the solid-state 'wetting angle' for a specific value of the dihedral angle. One boundary in this diagram represents the condition (values of D/t and wetting angle) where the free energy of the coherent film (represented by hexagonal, truncated grains) is equal to that of the film broken into isolated, single crystal islands (spherical caps). A third configuration also exists where

grains are still joined by grain boundaries, but the substrate is uncovered at triple points. As illustrated, the coherent film only exists over a small range of D/t. Also, for large wetting angles, only a small amount of grain growth will cause the coherent film to break into isolated islands at constant film thickness. For very thin films, only a small amount of grain growth is required to cause the polycrystalline film to break-up, uncover the substrate and reduce the free energy of the system.

For most film applications, the instability phenomenon is unwanted, i.e., either the film no longer covers and protects the substrate, the conducting strip line undergoes an instability and fails to conduct current, etc. On the other hand, if this break-up process occurs on a single crystal substrate with a dissimilar crystal structure relative to the structure of the thin film material, the resulting isolated grains, with a special orientation, can be used as 'seeds' to grow either a polyvariant or single crystal thin film as recently demonstrated by Miller and Lange.[8] In this method, material is re-deposited on the substrate containing the oriented, isolated grains; the 'seeds' consume the much smaller grains within the new deposition via grain growth.

3 Epitaxy of a Third Phase During Film - Substrate Reaction

Either polyvariant or single crystal thin films can form when the film reacts with a single crystal substrate. Examples of epitaxial reactions include MgA_2lO_4 (spinel) on basal plane sapphire[9] and $MgTi_2O_4$ on MgO single crystal substrates.[10] More recently Vaidya et al.[11] report the heteroepitaxy of several rare-earth hexa-aluminates ($LnAl_{11}O_{18}$ Ln = Nd, Gd) with the magnetoplumbite (mp) structure on basal plane sapphire with out-of-plane and in-plane orientation relations, $(0001)_{mp}\|(0001)_s$ and $<10\overline{1}0>_{mp}\|<11\overline{2}0>_s$, respectively.

The single crystal, rare-earth magnetoplumbite films are formed by coating a basal plane sapphire substrate with a precursor and heating to synthesize a polycrystalline rare-earth oxide film.[11] The reaction of the rare-earth oxide film with the substrate involves intermediate phases and their sequential epitaxy during each step of the reaction sequence. For the case of the Nd_2O_3 - Al_2O_3 reaction, phase equilibrium studies show that the binary system contains two phases, $NdAlO_3$ with a perovskite structure and the $NdAl_{11}O_{18}$ magnetoplumbite. The reaction/epitaxy sequence appeared as follows. After heat treatments at 800 °C, q-q XRD showed strong $(0002)_{Nd2O3}$ (hexagonal form of Nd_2O_3) diffraction, suggesting that the out-of-plane orientation of hexagonal-Nd_2O_3 with the basal plane sapphire of $<0001>_{Nd2O3}\|<0001>_s$.[12] Multiple in-plane orientations were observed in the pole figure

analysis for the same films. XRD showed that NdAlO$_3$ began to form via a Nd$_2$O$_3$/substrate reaction at temperatures as low as ~ 800 °C. When the films were heat treated to 1450 °C, pole figure analysis showed a different in-plane orientation relation, viz., <110>$_p$||<1210>$_s$.[12] SEM observations after the 1450 °C heat treatment showed that the NdAlO$_3$ grains were isolated islands on the basal plane sapphire substrate, consistent with the three, in-plane variants. The equilibrium out-of-plane and in-plane epitaxy relations, <111>$_p$||<0001>$_s$ and <110>$_p$||<1210>$_s$ shows that the oxygen planes of the perovskite epitaxy on the sapphire basal plane, and that the closed-packed, oxygen directions in the two structures are parallel to one another, viz., the oxygen plane stacking sequence is (...ababab)$_s$|interface|(abcabcabc.....)$_p$. The unrelaxed, in-plane strain for this epitaxial relation is ≈ 3 %.[12]

The second reaction, NdAlO$_3$ + 5Al$_2$O$_3$ → NdAl$_{11}$O$_{18}$, initiates at ≈ 1500 °C;[11] since the NdAl$_{11}$O$_{18}$ phase is not observed for long heat treatment periods at temperatures < 1450 °C, it appears not be a stable phase at lower temperatures as suggested by some phase equilibria studies. Since the rare-earth magnetoplumbites have a the cation ratio (Nd:Al) of 1:11 relative to the 1:1 for the perovskite, a much larger magnetoplumbite volume is formed relative to the isolated perovskite grains. Thus, as observed with the SEM and TEM,[11] when the NdAlO$_3$ grains are fully consumed, the NdAl$_{11}$O$_{18}$ reaction phase fully covers the sapphire surface as a single crystal thin film with an in-plane and out-of-plane epitaxial relation of <0001>$_{mp}$|| <0001>$_s$, <1210>$_{mp}$ || <1010>$_s$, respectively. The in-plane, unrelaxed lattice strain is ≈ 1 %. This epitaxial relation is very similar to that determined for the perovskite on basal plane sapphire, viz., the oxygen planes of the magnetoplumbite epitaxy on the sapphire basal plane and the closed-packed, oxygen directions in the two structures are parallel to one another. The difference is that the 6-fold rotational symmetry of the 'c' axes of the hexagonal magnetoplumbite structure allows it to overgrow the basal plane of sapphire with only one in-plane orientational relation. Thus, unlike the case of the rare-earth perovskite, the magnetoplumbites (rare-earth and otherwise) can form a true single crystal thin film (without in-plane variants) via the reaction epitaxy route.

4 Epitaxial Grain Growth: Identical Structures and Small Lattice Mismatch

When the film and substrate have identical structures, despite different chemistries, and their lattice mismatch strain is small (e.g., < a few percent), the epitaxy that accompanies grain growth does not involve the instability phenomena described above. Two well studied cases

will be review here: one where cubic zirconia containing different amounts of yttrium in solid-solution is epitaxied on a cubic (100) zirconia substrate,[13] and the other is the epitaxy of the perovskite, $PbTiO_3$, on a (100) cubic-perovskite $SrTiO_3$ substrate.[14] In the former case, the grain growth occurs by an irregular 'grain boundary' that slowly moves from the interface through to the surface to consume the polycrystalline film. In the latter case, the film first crystallizes with a metastable crystalline structure, and the epitaxy phenomena occurs rapidly over small temperature range concurrent with the structural transformation.

Miller et al. [14] studied the formation of single crystal thin films of cubic ZrO_2 (6 to 40 mol% Y_2O_3) on (100), cubic ZrO_2 (9.5 mol% Y_2O_3) substrates, using aqueous precursor solutions of zirconium acetate and yttrium nitrate. Film compositions within this range of Y_2O_3 solid-solution had a lattice mismatch up to 1.59%. The mechanism leading to the formation of a single crystal film from the initial, low density, nanometer crystallite thin film was detailed via TEM studies of cross-sectioned specimens. The TEM observations are schematically summarized in Fig. 2. For films heat treated at 600 °C, nano-meter crystallites (2 to 5 nm) in contact with the substrate were observed to have the same orientation as the substrate, whereas other crystallites (same size) in the porous network had no preferred orientation. At 700 °C, the porous film appeared denser and grains within this network became larger, but the epitaxied crystallites at the interface did not significantly alter. At 900 °C, a dense, epitaxial, single crystal layer (25 to 35 nm thick) was observed to have grown from the substrate interface into the polycrystalline film, which at this temperature, appeared much denser and contained larger (10 nm) grains. The interface between the epitaxied film and the polycrystalline film was irregular and had collected porosity during the growth of the epitaxial layer.

Dark field imaging revealed regions within the epitaxial film with a slightly different orientation relative to the rest of the film and the substrate. These regions had the polygonal shape and size of grains within the adjoining polycrystalline film. At 1100 °C, the epitaxial single crystal layer ($\approx$ 150 nm thick) had grown to the surface, viz., the polycrystalline portion was completely consumed. Other than a few threading dislocations, few defects were observed within the epitaxial film. The surface of the epitaxial film contained hemi-spherical pits, which appeared to be remnants of the pores driven in front of the epitaxial layer as it consumed the polycrystalline portion. Planar sections of this film revealed a dislocation network at the film-substrate interface. The spacing of dislocations within this network was consistent with lattice strain determinations via x-ray diffraction that $\approx$ 70 % of the differential

lattice strain (0.81 %) was relaxed. The surfaces of films heat treated at higher temperatures were smooth and featureless suggesting that the hemispherical surface pits had been eliminated via surface diffusion.

The TEM observations, summarized in Fig. 2, showed that the single crystal thin film developed by epitaxial grain growth. These observations also indicated that the grain growth phenomenon was hindered by porosity within the polycrystalline portion of the film. Namely, although the growth of the epitaxial film initiated with oriented, nano-meter grains at the substrate-film interface during precursor crystallization ($\approx$ 450 °C), the oriented grains could not consume the film grains until heat treatment at a higher temperature where the polycrystalline film became sufficiently dense to support grain boundary motion.
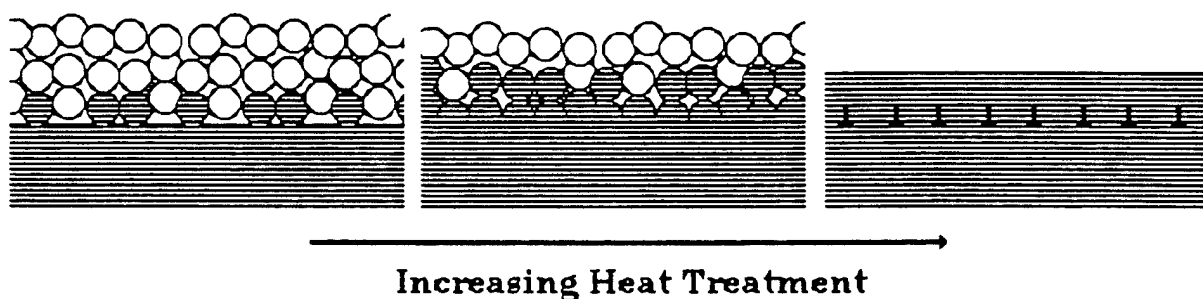

Increasing Heat Treatment

Figure 2 Schematic of epitaxial grain growth for a cubic s.s. $Zr(Y)O_2$ film composition (25 mole % Y_2O_3) on cubic s.s. $Zr(Y)O_2$ (9.5 mole % Y_2O_3) single crystal substrates ([100] orientation) as observed via crossectional TEM observations. [13]

In another study,[14] a mixed alkoxide liquid precursor was used to form epitaxial $PbTiO_3$ thin films by spin-coating on cubic (100) $SrTiO_3$ substrates. The films were heat-treated at temperatures between 380°C/1h and 800°C/1h. X-ray diffraction, atomic force microscopy, scanning and transmission electron microscopy were used to characterize the microstructure of the films and to evaluate the epitaxial phenomena. At ~400°C/1h, a polycrystalline, metastable fluorite structure crystallized from the pyrolyzed, amorphous precursor. At slightly higher temperatures (~420°C/1h), the thermodynamically stable phase, a perovskite epitaxially nucleated at the film/substrate interface. As schematically illustrated in Fig. 3, a small number of epitaxial grains grow through the film toward the surface and consume the nano-crystalline fluorite grains. Coarsening of the perovskite grains leads to a reduction in mosaic spread during further heating. Pores, that concurrently coarsen with grain growth, produce a pitted surface as they disappear from within the film. At 800°C/1h a dense epitaxial $PbTiO_3$ film with a smooth surface shown in Fig. 4. Figure 4 also shows that the

film, which epitaxies with a cubic perovskite structure above its Curie temperatures (≈ 480 °C), is tetragonal with the 'c' normal to the interface and contains laths of 'a' axis domains that help relieve the strain energy due to the structural phase transformation during cooling.
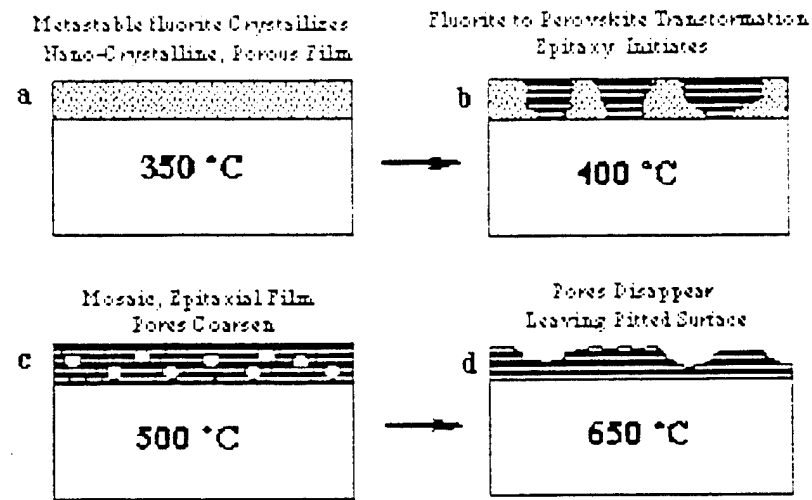

Figure 3 Schematic of PbTiO₃ epitaxy on SrTiO₃ single crystal substrate from a mixed-alkoxide solution precursor: a-d, different heat treatment temperatures for 1 h.[14]

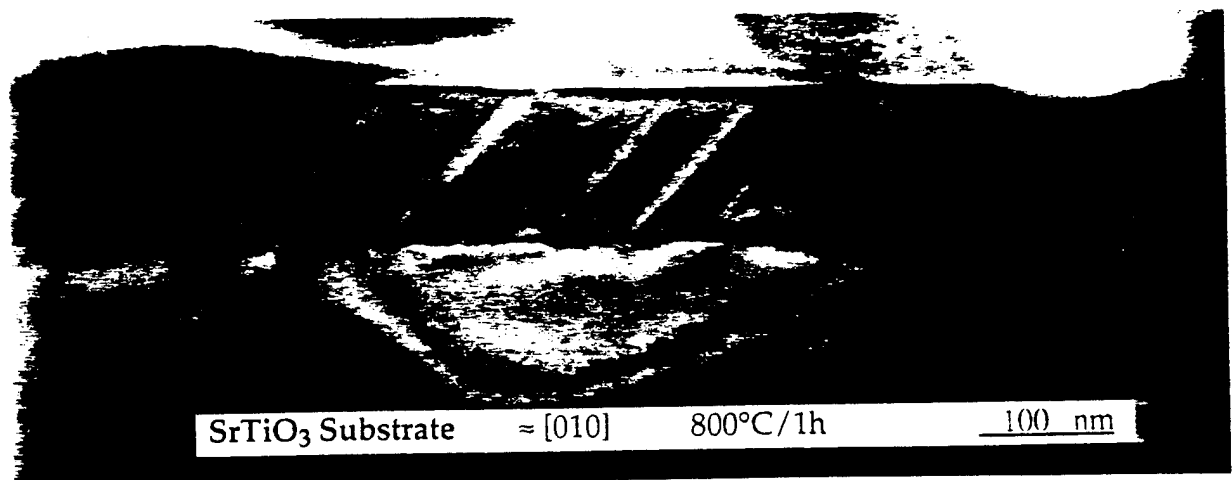Figure 4 TEM micrograph for PbTiO₃ single crystal thin film on SrTiO₃ single crystal substrate after heated at 800 °C for 1h. Film is predominately a 'c' axis domain ('c' axis of tetragonal PT perpendicular to interface); 'a' domains are laths at ≈ 45° angle.[14]

The observed epitaxy phenomenon of $PbTiO_3$ on $SrTiO_3$ is very different than that studied by Miller et al.[13] for solution derived cubic-ZrO_2 on cubic-ZrO_2 substrates. Although the initial crystallization was similar to that observed here, namely, the film directly crystallized into partially dense nano-crystalline ZrO_2, two phenomena were very different. First, the ZrO_2 nano-crystallites formed during crystallization had the same structure as the underlying substrate. Second, the nano-crystallites touching the substrate had the same crystallographic orientation as the substrate. It was these oriented crystallites that first grew across the film/substrate interface and then grew up to the film surface to produce a uniform conversion to a single crystal film. The driving force for this conversion was the free energy change associated with elimination of grain boundary energy per unit volume.

In the $PbTiO_3$ study,[14] the initial polycrystalline film did not have the same structure as the substrate, and the driving force for the nucleation and growth of the epitaxial grains was different. From the crystallization sequence, it is concluded that the initial crystallization of the metastable fluorite phase selectively *promotes* the perovskite epitaxy. In systems that directly transform into the final polycrystalline phase, elimination of grain boundary area is the only driving potential for the growth of the epitaxial film. In the case of the $PbTiO_3$ epitaxy, the fluorite to perovskite transformation provides an *additional* driving potential for epitaxial growth. This phase transformation takes place over a narrow temperature range and it leads to textured $PbTiO_3$ films at 450°C/1h, which is below its ferroelectric transformation temperature and at ~ 0.4 of its melting temperature. As described above, a relatively small number of perovskite grains with the same orientation as of the substrate were observed to grow through to the film surface and consume the nano-crystalline, metastable fluorite phase. It appeared that this additional driving potential not only allows a few large grains to rapidly grow through the polycrystalline film, but also leads to entrapped porosity within the growing, epitaxial grains. Thus, the higher driving potential for converting the polycrystalline film of one phase into an epitaxial film of a second phase appears to be, in-part, responsible for entrapped porosity and the less ordered growth of the single crystal thin film.

The large mosaic spread in the initially crystallized perovskite phase cannot be attributed to mosaic spread in the STO substrate but rather must be a consequence of the growth process. Since the transforming perovskite grains are growing into a partially dense polycrystalline fluorite matrix (which is also densifying during the phase transformation), it can be expected that each growing perovskite grain may be rotated, by a small amount, through differential densification. Differential densification of a powder matrix is common in composite systems

and produces rotations of individual grains and groups of grains.[15] In the current case, the growing perovskite grains can be considered as the inclusions (or reinforcements) within the low density matrix.

The entrapped pores coarsen when the films are heat-treated at higher temperatures. After heating to temperatures in excess of 675°C/1h, the pores disappeared from within the epitaxied film and the surface becomes pitted. Since pore disappearance requires material transport form the surface to the pore, or conversely, vacancy transport from the pore to the surface, it is obvious that the pits on the surface are the displaced pores from within the film. Heating to 800°C/1h (T $\approx$ 0.69 T$_{melting}$ of PbTiO$_3$) is required to produce sufficient long-range surface mass-transport to form an epitaxial film with a smooth surface as shown in Fig. 4.

5 Concluding Remarks

It is obvious that high quality, single crystal thin films can be produced via the solution precursor approach. Commonly referred to as the 'beakers and benches' method, it does not require expensive capital equipment usually associated with vapor deposition methods. In addition, as reviewed above, the phenomena responsible for epitaxy is generally associated with grain growth and different than those associated with vapor phase epitaxy.

Acknowledgment

6 References

[1] F. F. Lange, *Chemical Processing of Advanced Materials, Chemical Processing of Advanced Materials,* Ed. by L.L. Hench and J.K. West, pp 611-26, John Wiley and Sons (1992)

[2] D.K. Leung, C.J. Chang, M. Ruehle, and F.F. Lange, J. Am. Cer. Soc., 74 (11), 2786 (1991)

[3] M.L. Balmer, F.F. Lange, and C.G. Levi, J. Am. Cer. Soc., 75 (4), 946 (1992)

[4] C.V. Thompson, Annu. Rev. Mat. Sci., Vol. 20, 245-68 (1990)

[5] C.V. Thompson, J. Floro and H.I. Smith, J. Appl. Phys., 67 [9] 4099-4104 (1990)

[6] D.J. Srolovitz and S.A Safran, J. Appl. Phys., 60 [1] 247-60 (1986)

[7]   K. T. Miller, F. F. Lange, and D. B. Marshall 151 - 160 J Mat. Res. 5 (1990)

[8]   K.T. Miller and F.F. Lange, J. Mat. Res. 6 (11), 2387 (1991)

[9]   L. Navias J. Am. Ceram. Soc. 44, 434 - 436 (1961)

[10]   D. Hesse and H. Bethge J. Cryst. growth 65, 69 -76 (1983)

[11]   K. Vaidya, C.Y. Yang, M. de Graef, and F.F. Lange,J. Mat. Res. 9 (5), 410 (1994)

[12]   K. J. Vaidya and F. F. Lange, "Epitaxial Relations of $NdAlO_3$ Perovskite on Basal Plane Sapphire," submitted to J. Mat. Res. (1994)

[13]   K. T. Miller, C.-J. Chan, M.G. Cain, and F. F. Lange, J. Mat. Res. 8 (1), 169 (1993).

[14]   A. Seifert, F. F. Lange and J. S. Speck, "Epitaxial Growth of $PbTiO_3$ Thin Films on (001) $SrTiO_3$ from Solution Precursors," sent to J. Mat. Res.

[15]   O. Sudre and F.F. Lange, J. Am. Cer. Soc., 75 (3), 519 (1992).

Nano-Structures via Diffusion Limited Crystallization
from Solution Precursors: Synthesis and Properties

Contract AFOSR F49620-94-1-0229

Final Report

and Technical Report No. 2

period: April 15, 1994-April 14, 1995

MICROSTRUCTURAL INSTABILITY IN SINGLE CRYSTAL THIN FILMS

A. Seifert, A. Vojta, J.S. Speck, and F.F. Lange

Materials Department
College of Engineering
University of California, Santa Barbara
Santa Barbara, CA 93106

Microstructural Instability in Single Crystal Thin Films

A. Seifert, A. Vojta, J.S. Speck, and F.F. Lange

Abstract

Epitaxial $PbTiO_3$ thin films were produced from a mixed Pb-Ti-double-alkoxide precursor by spin-coating onto single crystal (001) $SrTiO_3$ substrates. Heat-treatment at 800°C produces a dense and continuous, epitaxial lead titanate film through an intermediate Pb-Ti-fluorite structure. A microstructural instability occurred when very thin single crystal films were fabricated; this instability caused the films to become discontinuous. Scanning electron microscopy and atomic force microscopy observations show that single crystal films with a thickness less than ~80 nm developed holes that expose the substrate; thinner films broke up into isolated, single crystal islands. The walls of the holes were found to be (111) perovskite planes. A free energy function, which considered the anisotropic surface energies of different planes, was developed to describe the microstructural changes in the film and to understand the instability phenomenon. The function predicted that pre-existing holes greater than a critical size are necessary to initiate hole growth and it predicted the observed morphological changes in the current system. Morphological stability diagrams that explain the stability fields for different film configurations, i.e., either completely covered, with holes, or single crystal islands, can be calculated for any film/substrate system.

1. Introduction

It is generally assumed that thin films will remain stable during their use. However, it has been shown that continuous films are not always thermodynamically stable and that they can uncover the substrate during a high temperature heat treatment. This phenomenon has been observed for a wide range of polycrystalline metal films.[1-7] Theoretical treatments for polycrystalline films have been reported by Srolovitz and Safran[8,9] as well as Miller *et al.*[10] for the case were the surface energy of the crystalline film is assumed to be isotropic. Miller *et al.* observed the breakup phenomenon for yttria-stabilized zirconia films on sapphire. They confirmed the hypothesis made by Srolovitz and Safran that grain boundary grooving can initiate the instability when the grain-size to film-thickness ratio exceeds a critical value.

A similar phenomenon was observed in this work for the case of epitaxial $PbTiO_3$ thin films grown on (001) $SrTiO_3$ by the solution precursor method.[11] As previously shown,[11] continuous and dense single crystal lead titanate films, ~120 thick, were prepared by depositing two layers of a Pb-Ti double-alkoxide precursor on $SrTiO_3$ substrates with an intermittent drying period of approximately two minutes. Subsequent heat-treatment in a PbO-environment at 800°C/1h transformed the precursor film to a single crystal $PbTiO_3$ film with the same orientation as the $SrTiO_3$ substrate. The conversion from a precursor film to a single crystal film during heat-treatment sequentially involved: *(i)* decomposition of the precursor, *(ii)* its crystallization to a nanocrystalline, metastable Pb-Ti-fluorite phase, *(iii)* transformation of the polycrystalline fluorite to large-grained, highly oriented perovskite, and *(iv)* grain growth to a dense, single crystal film with the same orientation as the underlying substrate.[11]

3

When films with a nominal thickness of less than ~100 nm were produced, as they underwent their conversion to a single crystal, they also developed holes which, upon further heating, either grew to a stable size or caused the film to break-up into isolated, single crystal islands. That is, as thinner films were produced, they became unstable and uncovered the substrate despite their single crystal nature. It was recognized that these phenomena were dependent on the film thickness. It was also found that the surfaces of the holes had a different crystallographic orientation relative to the film surface, suggesting that the surface energy anisotropy strongly influenced hole growth. As reported here, systematic experiments and analytical modeling were performed to develop a better understanding of the origin of the instability phenomenon.

2. Experimental Procedure

Lead Titanate films were prepared by spin-coating (001) strontium titanate substrates with a Pb-Ti-solution-precursor. Prior to deposition, the single crystal $SrTiO_3$ substrates (Coating & Crystal Technology Inc., Kittaning, PA) were thoroughly cleaned with organic solvents and subsequently thermally annealed at 1400°C/1hr to remove any polishing damage and to obtain a reproducible surface finish. The synthesis of the double-alkoxide precursor solution followed the method reported by Gurkovich and Blum[12] and is detailed elsewhere.[11] The original Pb-Ti-precursor was assayed and shown to contain 0.55 molar in $PbTiO_3$. As previously shown,[11] epitaxial $PbTiO_3$ films, ~120 nm thick, were prepared by depositing two layers of the precursor on $SrTiO_3$ substrates with an intermittent drying period of about two minutes. Subsequent heat-treatment in a PbO-environment to 800°C/1h

4

transformed the gel-like amorphous precursor film, via pyrolysis and crystallization, to the epitaxial $PbTiO_3$ layer.

Lead titanate films, with a smaller thicknesses compared to those previously grown (hereon referred to as the *standard thickness*; ~120 nm), were prepared in this study. Films one half (~60 nm) of the standard film thickness were prepared by depositing only *one* coat of the precursor solution. Thinner films, one quarter (~30 nm) and one eighth (15 nm) of the standard film thickness, were made by diluting the 0.55 molar stock-precursor solution with anhydrous 2-methoxy ethanol and applying one coat of this diluted precursor to the (001) $SrTiO_3$ substrates. After deposition and drying for 30 minutes in air the precursor films were heated in a tube-furnace under flowing oxygen (~12 cm^3/min) at 5°C/min to temperatures between 600°C and 800°C, using a PbO-environment to avoid lead-loss.[11] Evolution of the microstructural was characterized with Scanning Electron Microscopy (SEM; JEOL 6300FE, Tokyo, Japan) and Atomic Force Microscopy (AFM; Nanoscope III, Digital Instruments Inc., Santa Barbara, Ca). AFM was also used to perform height- and section-analysis on the layers and x-ray diffraction (XRD, XDS2000, Scintag Inc., Sunnyvale, CA, and MRD, Philips, Eindhoven, The Netherlands) was used to confirm the epitaxial nature of the films.

3. Results

Continuous and dense single crystal lead titanate films were prepared by depositing two layers of a Pb-Ti double-alkoxide precursor on $SrTiO_3$ substrates.[11] Heat-treatment at 800°C/1h yielded epitaxial single crystal $PbTiO_3$ films with a thickness of ~120 nm as shown in the AFM micrograph in Fig. 1.

X-ray pole figures of films $1/2$, $1/4$, and $1/8$ of the standard thickness, heat-treated at 800°C/1h, showed that the films were epitaxial with the same orientational relation, $\{001\}[100]_{PbTiO3}||\{100\}[100]_{SrTiO3}$, previously reported.[11] AFM characterization of a $1/2$-standard thickness specimen produced at 800°C/1h revealed that the film contains strongly faceted holes as shown in Fig. 2. The holes uncover ~30% of the substrate area. The average film thickness was determined by AFM to be ~100 nm, *i.e.*, thicker than that expected if the film was continuous. The intersection traces of the faceted holes with the substrate were determined to be nearly parallel to $[110]_{SrTiO3}$, leaving two possibilities for low-index facet-plane orientations, namely, either (111), if the surfaces of the hole were inclined with respect to the substrate, or (110) if the surface of the hole was perpendicular to the substrate. An AFM section-analysis was performed along line A in Fig. 2. Accounting for the pyramidally shaped AFM tip used in the scan, the inclination angle of the pore surface was shown to be 54° relative to the substrate normal. Since the angle between the (111) and (100) planes in a cubic material is 54.73°, it was concluded that the pyramidal facets were indeed (111) surfaces. More evidence that the hole surfaces were (111) surfaces is shown in Fig. 3 where a pit in a standard thickness film (~120 nm) is faceted at the bottom. The ferroelectric domains that are also imaged in Fig. 3 have {101} twin planes with surface traces along [100] and [010]. Using the known geometry of the twins and their geometric relation to the faceted pit, the facet surfaces were again determined to be {111} planes.

For films of $1/4$ the standard thickness, heat-treated at 800°C/1h, the uncovered substrate area increases to ~42%. SEM showed that the film is still continuous and AFM section-analysis recorded an average height for the covered areas of approximately 50 nm.

The AFM micrograph of a $1/8$-standard thickness film in Fig. 4 shows that during the heat-treatment to 800°C/1h, this thinner film entirely breaks up into islands, uncovering ~70% of the substrate. The average height of the islands was determined by AFM section analysis to be 60 nm.

In a second set of experiments a $1/2$-standard thickness film was heated to increasing temperatures to observe its microstructural evolution. This was accomplished by observing several specific areas of the film by low-voltage SEM after each heating cycle. As shown in Fig. 5a, the microstructure after heating to 600°C/1h consisted of some large grains that have grown abnormally to ~0.5 μm and are embedded in a porous film that appears to be polycrystalline. Arrows mark the same position for consecutive images. Fig. 5b shows that heating to 650°C/1h changes the morphology to a rough, strongly pitted and faceted, epitaxial film with residual grains and pores that in some cases appear to expose the substrate. All areas showing residual grains and large pores in the film at 650°C/1h can be related to large grains present at 600°C/1h (see markers). Increasing the heat-treatment temperature to 700°C/1h leads to a smooth film surface with residual small pits. Additionally, heat-treatment at this temperature lead to significant growth of holes observed at the lower temperature, as shown in Fig. 5c. The walls of the holes are strongly faceted with most of their traces along [110] or [$\bar{1}$10] directions as previously described. Continued heating to 750°C/1h leads to further growth and coarsening of the porosity. Smaller pores and pits present at lower temperatures, that did not penetrate to the film/substrate interface, *disappear* during the heat treatment at 750°C as shown in Fig. 5d. It is important to note that the hole configuration stabilizes during heating at 800°C/1h and no further change was detectable after further heating to 850°C/5h.

4. Free Energy Function for Film Instability

The experimental observations appear to connect the microstructural instability of epitaxial thin films to the film thickness. Namely, relatively thick films were found to cover the substrate completely, whereas thinner layers may develop substrate-exposing pores. For even thinner films, the holes appear to grow until they overlap and cause the film to break up into isolated islands. It was also found that small pits that do not expose the substrate, as well as relatively small holes that do expose the substrate, will not grow, but instead, disappear during heating. The disappearance of pits in thin films is consistent with results of an early study by Herring[13] on the stability of flat surfaces of solids with anisotropic surface energy. Later Mullins[14] showed that a film with an isotropic surface energy is stable against the growth of surface perturbations.

Our study on single crystal films has similarities to previous work on polycrystalline films. Srolovitz and Safran[8] found that large amplitude perturbations at triple points will grow into holes if the film thickness to grain size ratio is smaller than a critical value. In that work the instability phenomenon was shown to be the result of grain boundary grooving at three-grain junctions. The instability phenomenon associated with polycrystalline films was further studied with experiments on polycrystalline $Zr(Y)O_2$ films containing 8 mol% Y_2O_3 grown on single crystal Al_2O_3 substrates.[10] Here, larger grains grew by boundary motion to consume smaller grains and then spheroidize to uncover the substrate at triple points. A free energy model showed that this phenomenon only occurred when the grain size to film thickness ratio becomes larger than a critical value.

The growth of isolated pores in thin films with isotropic surface energies is described in a recent review by Srolovitz and Goldiner.[15] They showed that if the hole surface to film surface energy-ratio was less than a critical value, an isolated hole would grow without bounds to completely uncover the substrate. It was found that Srolovitz and Goldiner's analysis was inconsistent with the observations reported here because they only treated the case of a single isolated hole that can grow without bounds, whereas the films observed in this study contain many holes and each can grow to a stable size. As we show below, when the spacing between the holes is finite, volume conservation causes the thickness of the film to increase concurrent with hole growth. It was thus realized that the increasing film thickness is important in determining the configuration of the film during hole-growth.

The free energy calculations of our study show that anisotropic surface energies are necessary to describe the morphological changes in the film during hole-growth. The problem of the equilibrium morphology of an *isolated* single crystal island with *anisotropic* surface energy was treated by Winterbottom.[16] In this analysis the surface energy of the crystalline islands was minimized, at constant volume. Winterbottom's analysis showed that the morphology of the island is determined by a generalized Gibbs-Wulff construction, which is similar to the Gibbs-Wulff construction of a free standing particle.[17] The Gibbs-Wulff construction for the island includes both the film-substrate interfacial energy γ_i and substrate surface energy γ_s. In the general case, the island will be faceted due to anisotropic surface energies and thus, a wetting angle cannot be defined. Rather, the "wetting" behavior depends on the stable facets and determines the equilibrium shape of the

9

island which usually is given by the height to width ratio as described in Appendix II.

The Winterbottom approach treats the global surface energy minimization of an isolated volume of material on an infinite substrate. Although, as described in Appendix II, this approach is appealing to our problem, we describe a thermodynamic function that deals with the growth of initially isolated holes, separated by a fixed distance, in a film of finite thickness. This approach not only is more appropriate to our problem where holes were observed to grow to either a fixed area ratio or produce isolated islands, but it is also consistent with solution precursor processing which inherently involves the formation of pores when a low density, porous network of nano-crystallites during low temperature pyrolysis and crystallization.[18] In the formation of single crystal films, densification as well as grain- and pore-growth are concurrent. The kinetics of these processes and the development of the holes in partially epitaxied films are dependent on a number factors, including the precursor characteristics, which are beyond the scope of this work. In our modeling, we consider two important dimensions associated with the single crystal film and the holes - 'h_0', the thickness of the single crystal film without holes, and 'a', the separation distance between holes.

4.1 General Free Energy Expressions

A three dimensional free energy analysis was carried out to understand the instability phenomenon observed in epitaxial films as a function of film thickness and the relative interfacial energies. The analysis presented here shows that the spontaneous growth of surface pits into holes, which may or may not further grow to uncover the substrate, not only depends on the

10

relative values of the different interfacial energies, but also depends on the initial size of the holes *and their spacing*. The physical reason for the dependence on the spacing is that as the hole grows, its mass must be redistributed to increase the film thickness. Increasing the film thickness increases the surface area of the hole. If the spacing is very large relative to the hole size, the effect of film thickening can be neglected. But as shown below, when the spacing is similar to experimental observations, the effect of spacing leads to the instability phenomenon. The effect of the initial hole size is also important because, for certain regimes of relative interfacial energies, a critical hole size is necessary for spontaneous growth. Physically, the mean spacing between pores is governed by a variety of kinetic factors mentioned in the previous section. For the analysis, this should be treated as an experimentally observable quantity.

Our analysis considers a single crystal film of initial thickness h_0, divided into square unit cells of dimension a, as shown in Fig. 6. The growing pores are placed at the corners of the unit cell and thus, the cell dimension, a, corresponds to the average pore separation distance. The analysis initiates with the growth of a tetragonal, pyramidal pit with surfaces that form an angle α with the film surface, as shown in Fig. 6.

It is convenient to divide the free energy analysis into four different regimes shown in Fig. 6: *(i)* the 1st regime describes the growth of pyramidal holes at the corners of the unit cell until they reach the film/substrate interface (Fig. 6a); *(ii)* in the 2nd regime, the holes continue to grow with the shape of truncated pyramids until their upper edges, b, intersect the sides of the unit cells at $a/2$ ($b = a/\sqrt{2}$) as shown in Fig. 6b. *(iii)* In the 3rd regime, the continuity of the film can be described by truncated pyramids with cut-off corners. As the holes continue to grow, the cut-off corners become smaller,

11

until at the end of this regime, the film section is shaped like a truncated pyramid. At this point, each portion of the film is only connected to every other portion at its lower edges, c, *i.e.*, c now intersects the unit cell edge at $a/2$ and $c = a/\sqrt{2}$, as shown in Fig. 6c; *(iv)* in the 4th regime the film is no longer connected and the remaining islands can be described as truncated pyramids, as illustrated in Fig. 6d. The geometrical parameter used to describe the hole-growth through all four regimes is x, which is one half of the diagonal of the growing hole at the film surface as shown in Fig. 6.

The general free energy expression, E, of the film/substrate system is given by

$$E = A_t\, \gamma_t + A_p\, \gamma_p + A_i\, \gamma_i + A_s\, \gamma_{s,,} \tag{1}$$

where γ is the surface energy per unit area, A the area, and the subscripts denote the film surface (t), the pyramidal (or hole) surface (p), the film/substrate interface (i) and the uncovered substrate surface (s). In each of the regimes discussed above, the respective free energy functions include a term for each of the surfaces/interfaces that change during the growth of either the pit or hole. As shown later, the values of the free energy functions each regime are continuous across the geometrical boundary where one regime ends and the next begins. The expressions for the different areas, A_t, A_p, A_i, *and* A_s, film volumes, and heights h of the film, which depend on the hole size x, are given in Tables I, II and III, respectively, for all four regimes. Because the film volume is conserved during hole growth (Table II), the film thickness h concurrently increases with increasing hole size x, as shown in Table III.

4.2 Regime 1, Growth of Pyramidal Pits

The free energy E_1 is normalized by the initial free energy of the film, $E_0 = a^2(\gamma_t + \gamma_i)$, without any holes. $\overline{E}_1 = E/E_0$ is evaluated as a function of the increasing hole size, x, by substituting the proper area functions and film thickness expressions found in Table I and III into eqn. (1) to obtain

$$\overline{E}_1 = 1 - 4\frac{\delta^2}{a^2}\frac{1}{tan^2\,\alpha}T + 4\frac{\delta^2}{a^2}\frac{1}{tan\,\alpha\,sin\,\alpha}P, \qquad (2)$$

where $\delta = \left(h - h_0 + \dfrac{x\,tan\,\alpha}{\sqrt{2}}\right)$, $T = \dfrac{\gamma_t}{\gamma_t + \gamma_i}$ and $P = \dfrac{\gamma_p}{\gamma_t + \gamma_i}$. (3)

From the expressions in Table III, we can see that h is a function of x, h_0 and α and thus, $\overline{E}$ is a function of x, h_0, α, T and P. The free energy change in regime 1 can be viewed when either the surface energy ratio γ_p/γ_t is varied and α is fixed, as shown in Fig. 7, or where α is varied and γ_p/γ_t is fixed.

For the case where γ_p/γ_t is varied, α was set to 54.7°, consistent with observations of the (111) pyramidal facets reported above. As shown in Fig. 7, the normalized free energy increases for all ratios of $\gamma_p/\gamma_t > 0.577$, indicating that for greater ratios, it is energetically unfavorable for pits to exist in a single crystal film. However, pits can spontaneously grow when the γ_p/γ_t ratio is ≤ 0.577, where the normalized free energy $\overline{E}_1$ is ≤ 1 for all x/a, as given by

$$4\frac{\delta^2}{a^2}\frac{1}{tan^2\,\alpha}T = 4\frac{\delta^2}{a^2}\frac{1}{tan\,\alpha\,sin\,\alpha}P. \qquad (4)$$

13

For the second case, α was allowed to vary and, for reasons discussed below, γ_p/γ_t was assumed to be 0.8. One can show that for a fixed ratio of $\gamma_p/\gamma_t = 0.8$, a pyramidal pit can only grow if $\alpha < 36.8°$.

If the specific case of $PbTiO_3$ on $SrTiO_3$ is considered, the ratio γ_p/γ_t can only vary within bounds determined by the equilibrium shape of a crystal, as given by a Wulff plot.[17] In this three dimensional diagram, the surface energy γ is radially plotted as a function of crystallographic plane normals. Minima, or cusps, occur in the plot for lower energy planes. The equilibrium shape is then determined by the locust of inner tangent planes to the radial surface energy "vector" and is usually governed by the location of the deepest cusps in the plot. Fig. 8 illustrates the schematic development of such a three-dimensional plot in a cross-section. For the case of $PbTiO_3$ films, experimental results suggest that two surfaces are stable: the (100) surface with a surface energy per unit area of γ_t, and the (111) surface with a surface energy per unit area of γ_p. Geometrical considerations, given in the schematic of Fig. 8, dictate that both (100) and (111) are stable provided

$$0.577 < \gamma_p/\gamma_t < 1.73. \tag{5}$$

For $\gamma_p/\gamma_t > 1.73$ only the (100) surface is stable. Like-wise, when $\gamma_p/\gamma_t < 0.577$, only the (111) surface is stable. From the graph in Fig. 7 it can be seen that within the bounds where both (111) and (100) are stable ($0.577 < \gamma_p/\gamma_t < 1.73$), the growth of a pyramidal pit is not favored. This is entirely consistent with the early work on stability of surfaces against microfacetting by Herring, who showed that thermodynamically stable surfaces are stable against small amplitude perturbations.[13]

14

For both cases shown (*i.e.*, variable γ_p/γ_t and variable α), the initial normalized film thickness h_0/a (normalized by the unit-cell size a) does not influence the formation and growth of the pyramidal pits. Therefore, the function for $\overline{E}_1(x)$ is identical for all h_0/a. However, h_0/a *does* determine the condition when the growing pit would intersect the film/substrate interface, defining the transition to regime 2. This condition is fulfilled when

$$\frac{x_{max1}}{a} = \frac{h_0}{a} \frac{\sqrt{2}}{\tan\alpha} . \qquad (6)$$

The condition where the pit intersects the film/substrate interface is shown in Fig. 7 by the change from continuous to dashed line for each of the free energy curves for the initial condition of $h_0/a = 0.1$. A second condition for the end of regime 1 exists when the upper edges b (see Fig. 6) of the growing pyramidal pits intersect the unit cell edge at $a/2$ before the pyramid tip can reach the film/substrate interface, *i.e.*, $b = a/\sqrt{2}$. This condition applies to relatively thick films and when α is shallow. x_{max1} for this case can be determined with

$$\frac{x_{max1}}{a} = \frac{1}{2} + \frac{\sqrt{2}}{\tan\alpha} \frac{(h_0 - h)}{a} , \qquad (7)$$

where h is also a function of x.

4.3 Hole Growth and Island Formation

In this section the total free energy of all four regimes will be evaluated for a chosen set of boundary conditions that are consistent with those reported above for the single crystal $PbTiO_3$ epitaxial films on the $SrTiO_3$

15

substrates. This analysis will show how the presence of pre-existing holes and the value of the initial film thickness produces the observed configurations. The calculations of the free energy function (eqn. 1) for each of the four regimes was carried out by substituting the area functions from Table I and then normalizing the result with the initial energy of the unit cell, $E_0 = a^2(\gamma_t + \gamma_i)$. For the case of epitaxial PbTiO$_3$ films considered here, a value of 54.7° was used for α, which is the angle between the (111) facets of the pyramidal pit and the (100) film surface. γ_p/γ_t was set equal to 0.8 since (111) and (100) are both stable surfaces for PbTiO$_3$. γ_i/γ_t was assumed to be 0.1 because both PbTiO$_3$ and SrTiO$_3$ are both perovskite titanates with similar lattice parameters. In addition, the ratio of γ_s/γ_t was assumed to be 1.0, since both are stable (100) surfaces with similar chemical composition.

Figure 9 shows the normalized free energy dependence on the normalized hole size, x/a, for films with five different values of the normalized thickness h_0/a ranging from 0.015 to 0.05. Using the surface energy ratios and the value of $\alpha = 54.7°$, as discussed above, Fig. 7 shows that the free energy of a pyramidal pit always monotonically increases if it tries to grow (regime 1). However, if a hole pre-exists such that the substrate is already exposed (regime 2), then the influence of h_0/a becomes significant on whether or not the hole grows.

Assuming that a hole pre-exists within the film, it will be shown that different film configurations will be either meta-stable or stable depending on value of h_0/a. Three threshold values for h_0/a define the stability of the different configurations and were numerically determined from the maxima and minima of the free energy functions in all four regimes $\frac{d\overline{E}}{dx} = 0$:

(i) In the case of relatively thick films, the normalized free energy $\overline{E}$ rises monotonically through all four regimes. For the parameters chosen, and

16

$h_0/a > 0.038$, no pre-existing hole of any size can grow without increasing the free energy. Also, for this case, pre-existing holes will shrink and disappear. Consequently, the thermodynamically stable configuration is a continuous film without either pits or holes.

(ii) For very thin films where $h_0/a < 0.0225$, $\overline{E}$ first rises to a maximum in regime 2 before it decreases monotonically to a minimum in regime 4, where the stable configuration is that of isolated, single crystal islands. Islands form in the 4th regime because the x/a value of $\overline{E}_4$-minima is larger than the threshold value for hole-overlap, given by the transition from regime 3 to 4 (see Fig. 6):

$$\frac{x_{max 3}}{a} = \frac{1}{2} + \frac{\sqrt{2}}{\tan \alpha} \frac{h_0}{a} . \tag{8}$$

The maximum in regime 2 when $h_0/a \leq 0.0225$ (illustrated in Fig. 9 for the function where $h_0/a < 0.015$), indicates that a pre-existing hole can grow, provided it is equal or larger than a critical size. That is, if holes of a critical size do not pre-exist, the continuous film, without either pits or holes, is a metastable configuration.

(iii) For films with h_0/a between $0.0225 < h_0/a < 0.038$, free energy minima will exist in both, regime 2 (holes grow to a given size) and 4 (holes grow together to form single crystal islands), but an energy barrier exists between the two. Thus, if holes pre-exist with sizes greater than a critical value, they will grow to a size determined by the free energy minimum in regime 2. This is a meta-stable configuration since, although an energy barrier exists, the lowest free energy configuration would be either single crystal islands or a completely covered film. To determine

17

the thermodynamic stable configurations for this case, the h_0/a values have to be separated into two areas. The boundary for the two h_0/a-areas can be numerically determined to be $h_0/a = 0.031$ by finding this particular h_0/a value where $\overline{E}$ in regime 2 and 4 are equal at their respective local minima (Fig. 9). For films with $0.0225 < h_0/a < 0.031$ the lowest $\overline{E}$-configuration is represented by a film broken up into islands, because the lowest free energy minimum lies in regime 4; and for films with $0.031 < h_0/a < 0.038$ the lowest free energy is when $\overline{E} = 1$, *i.e.*, the configuration where the substrate is completely covered and the film contains no pits at $x/a = 0$. Below, we will show a case in which isolated holes are a stable configuration.

4.4 Stability Diagrams

A stability diagram can be constructed to explain the different configurations of a thin, single crystal film. Three thin film configurations are of interest: a) one where the film fully covers the substrate, b) another were the film contains adjacent holes that have grown such that the film is still contiguous but with holes that expose the substrate, and c) a third configuration where the holes have grown together so that the film only exists as isolated, single crystal islands. The lines that divide the stability diagram into these three regions are derived by determining the free energy minimum for the three configurations and their relative values for each set of variables, α, x/a, h_0/a, γ_p/γ_t, γ_i/γ_t, and γ_s/γ_t.[10] The stability diagram will occupy a multi-dimensional space.

To understand the stability diagrams it is best to examine 'slices' of the multi-dimensional stability areas of the different configurations. For this

purpose, values for the variables were chosen that we believe are representative of the PbTiO$_3$/SrTiO$_3$ (001) epitaxial system. Stability fields were mapped for varying: *(i)* γ_p/γ_t and normalized film height h_0/a; *(ii)* γ_i/γ_t and h_0/a; and *(iii)* γ_s/γ_t and h_0/a. Other variables are kept constant for the specific maps.

(i) A small slice of the stability diagram is shown in Fig. 10 for the same conditions used to obtain Fig. 9 but for γ_p/γ_t ranging between 0.6 to 1.8 (with $\alpha = 54.7°$, $\gamma_i/\gamma_t = 0.1$ and $\gamma_s/\gamma_t = 1.0$). The choice of these γ_p/γ_t values stems from considerations in the system SrTiO$_3$/PbTiO$_3$, as discussed in section 4.2. It was shown that both pyramidal (111) planes as well as film-top (100) planes are stable if $0.577 < \gamma_p/\gamma_t < 1.73$. The continuous curve in Fig. 10 separates the stability fields of films broken up into islands and films that completely cover the substrate. The dashed curves envelope the area in the diagram where meta-stable holes can occur because a local $\overline{E}$-minimum exists in regime 2. The areas where islands and completely covering films are meta-stable were not included in the diagram. The diagram shows that as the ratio of γ_p/γ_t increases, the stability regime of the completely covered film shifts to smaller h_0/a-values, indicating that thinner films are more stable against uncovering as the formation of facets (with γ_p) becomes energetically more costly.

Comparison of the model with experimental results shows good agreement. The PbTiO$_3$ films grown for this study were continuous at ~120 nm thickness and formed either meta-stable or stable holes (see below) for films of 60 nm nominal thickness (or one half of the standard value). Thinner films of ~$1/8$ of the standard thickness were observed to break up into islands. The model yields similar thickness ratios for configurations that

19

cover the substrate completely, form meta-stable holes, or form islands, as can be seen in the diagram in Fig. 10.

(ii) Another section through the stability space is shown in Fig. 11 for the variable γ_i/γ_t and h_0/a with other variables held constant as follows: $\gamma_p/\gamma_t = 0.8$, $\gamma_s/\gamma_t = 1.0$, and $\alpha = 54.7°$. A similar diagram results with the difference, that for $\gamma_i/\gamma_t > 0.15$ a thin region exists where holes are the thermodynamically stable configuration. For smaller values of the interfacial energy, a direct boundary exists between stable islands and a stable covered configuration. For heights above the values of the continuous line in Fig. 11 the stable configuration is a completely covered film. For h_0/a values lower than the continuous line, single crystal islands are stable. Similar to the diagram discussed above, an area exists where meta-stable holes exist, enveloped by the dashed curves. The areas for the meta-stable covered and island configuration are not included. For increasing γ_i/γ_t it can be seen that the stability range for holes and single crystal island configuration extends to larger values of h_0/a. This indicates that for large values of the interfacial energy the system prefers configurations that minimize the interfacial area and consequently hole- or island-configurations form.

(iii) In Fig. 12, a third section through the multi-dimensional stability diagram is mapped for the variables γ_s/γ_t and h_0/a with the other variables set to $\gamma_p/\gamma_t = 0.8$, $\gamma_i/\gamma_t = 0.1$, and $\alpha = 54.7°$. Again, the solid line separates stable islands and the stable completely covered configuration. Meta-stable holes exist within the dashed lines. It can be seen from the diagram in Fig. 12 that as the ratio of the substrate surface energy to the film-top energy increases, energetically it becomes decreasingly favorable to expose the substrate surface, and for a given h_0/a the configuration changes from island to hole to completely covered. Increasingly thinner films keep the substrate fully

covered as γ_s/γ_t increases and beyond $\gamma_s/\gamma_t = 1.1$ only complete coverage of the substrate is energetically favored. This also indicates that for the case of PbTiO$_3$ on SrTiO$_3$, γ_s/γ_t has to be lower than this value since meta-stable or stable holes were observed in the films. It also indicates that a value of $\gamma_s/\gamma_t = 1.0$ for the other calculations is reasonable.

5. Conclusions

A microstructural instability phenomenon was observed for epitaxial PbTiO$_3$ thin films on SrTiO$_3$ substrates. Experimental observations showed that three different film-configurations may exist, which depend on the film thickness: thick films completely cover the substrate whereas pre-exiting holes in thinner films can grow to either form a continuous film containing an equilibrium area faction of holes or grow together to cause the film to break-up into single crystal islands. A free energy model, which includes surface energy anisotropy and the spacing between pre-existing holes, was used to understand the instability. The model showed, similar to the experimental results, that pre-existing holes in thinner films tend to uncover the substrate. It was also found that for the range of surface energies consistent with the current system, pre-existing holes were necessary to initiate the instability. To evaluate the influence of the interfacial-, substrate-, film-surface, and hole-surface energies as well as the film thickness, stability maps were constructed that show the parameters governing the epitaxial film morphology

Acknowledgments

Tables

<table>
<tr><th colspan="3">Table I: Area Functions for the Free Energy Equation</th></tr>
<tr><th>Area</th><th>Initial</th><th>Regime 1</th></tr>
<tr><td>A_t</td><td>a^2</td><td>$a^2 - \dfrac{4\left(h - h_0 + (x\tan\alpha)/\sqrt{2}\right)^2}{\tan^2\alpha}$</td></tr>
<tr><td>A_p</td><td>0</td><td>$\dfrac{4\left(h - h_0 + (x\tan\alpha)/\sqrt{2}\right)^2}{\sin\alpha\tan\alpha}$</td></tr>
<tr><td>A_i</td><td>a^2</td><td>a^2</td></tr>
<tr><td>A_s</td><td>0</td><td>0</td></tr>
</table>

<table>
<tr><th colspan="2">Table I, continued</th></tr>
<tr><th>Area</th><th>Regime 2</th></tr>
<tr><td>A_t</td><td>$a^2 - \dfrac{4h^2}{\tan^2\alpha} - 2\left(x - h_0\sqrt{2}/\tan\alpha\right)^2 - \dfrac{4\sqrt{2}h(x - h_0\sqrt{2}/\tan\alpha)}{\tan\alpha}$</td></tr>
<tr><td>A_p</td><td>$\left(\dfrac{h}{\tan\alpha} + \sqrt{2}\left(x - h_0\sqrt{2}/\tan\alpha\right)\right)\dfrac{4h}{\sin\alpha}$</td></tr>
<tr><td>A_i</td><td>$a^2 - 2\left(x - h_0\sqrt{2}/\tan\alpha\right)^2$</td></tr>
<tr><td>A_s</td><td>$2\left(x - h_0\sqrt{2}/\tan\alpha\right)^2$</td></tr>
</table>

Area	Table I, continued
	Regime 3
A_t	$\left(a\sqrt{2} - \dfrac{2h}{\tan\alpha} - \sqrt{2}\left(x - h_0\sqrt{2}/\tan\alpha\right)\right)^2$
A_p	$\left(a\sqrt{2} - x\sqrt{2} + \dfrac{2h_0}{\tan\alpha} - \dfrac{h}{\tan\alpha}\right)\dfrac{4h}{\sin\alpha} - \dfrac{4\left(a/2 - x + h_0\sqrt{2}/\tan\alpha\right)}{\cos\alpha}$
A_i	$a^2 - 2\left(x - h_0\sqrt{2}/\tan\alpha\right)^2$
A_s	$2\left(x - h_0\sqrt{2}/\tan\alpha\right)^2$

Area	Table I, continued
	Regime 4
A_t	$\left(a\sqrt{2} - \dfrac{2h}{\tan\alpha} - \sqrt{2}\left(x - h_0\sqrt{2}/\tan\alpha\right)\right)^2$
A_p	$\left(a\sqrt{2} - \dfrac{h}{\tan\alpha} - \sqrt{2}\left(x - h_0\sqrt{2}/\tan\alpha\right)\right)\dfrac{4h}{\sin\alpha}$
A_i	$\left(a\sqrt{2} - \sqrt{2}\left(x - h_0\sqrt{2}/\tan\alpha\right)\right)^2$
A_s	$a^2 - \left(a\sqrt{2} - \sqrt{2}\left(x - h_0\sqrt{2}/\tan\alpha\right)\right)^2$

Regime	Table II: Volume Equations
1st	$a^2 h_0 = a^2 h - \dfrac{1}{3}\left(h - h_0 + \dfrac{x\tan\alpha}{\sqrt{2}}\right)b^2$
2nd	$a^2 h_0 = a^2 h - \dfrac{1}{3}h\left(b^2 + c^2 + \sqrt{b^2 c^2}\right)$
3rd	$a^2 h_0 = \dfrac{1}{3}h\left(b^2 + c^2 + \sqrt{b^2 c^2}\right) - 2\dfrac{1}{3}h_{co}A_{co}$
4th	$a^2 h_0 = \dfrac{1}{3}h\left(b^2 + c^2 + \sqrt{b^2 c^2}\right)$

Reg.	Table III: Equations for Film Thickness
1st	$h = a\tan\alpha\cos\left(\dfrac{ar\cos(-3x/a\sqrt{2})}{3} + \dfrac{4}{3}\pi\right) - \dfrac{x\tan\alpha}{\sqrt{2}} + h_0$
2nd	$h = a\tan\alpha\cos\left(\dfrac{ar\cos(y^3\sqrt{2}/a^3 - 3y/a\sqrt{2} - 3h_0/a\tan\alpha)}{3} + \dfrac{4}{3}\pi\right)$ $- \dfrac{y\tan\alpha}{\sqrt{2}}$
3rd	$h = \sqrt[3]{\left|\left(-\dfrac{3}{4}a^3 - y^3 + \dfrac{3}{2}a^2 y + \dfrac{3}{2}a^2 h_0 \dfrac{\sqrt{2}}{\tan\alpha}\right)\dfrac{\tan^3\alpha}{2\sqrt{2}}\right|} - \dfrac{y\tan\alpha}{\sqrt{2}} + \dfrac{a\tan\alpha}{\sqrt{2}}$
4th	$h = \sqrt[3]{\left|\left(-a^3 + y^3 + 3a^2 y - 3ay^2 + \dfrac{3}{2}a^2 h_0 \dfrac{\sqrt{2}}{\tan\alpha}\right)\dfrac{\tan^3\alpha}{2\sqrt{2}}\right|} - \dfrac{y\tan\alpha}{\sqrt{2}}$ $+ \dfrac{a\tan\alpha}{\sqrt{2}}$

with $y = \left(x - \dfrac{\sqrt{2}h_0}{\tan\alpha}\right)$

Appendix I: Notation

a unit cell size

α pyramidal angle

A area coefficient

b upper edge of pyramidal facet

c lower edge of pyramidal facet (on substrate)

co cut-off corner, index for volume in regime 3

δ $\delta = \left(h - h_0 + (x \tan\alpha)/\sqrt{2} \right)$

E total free energy

E_0 initial total free energy

$\overline{E}$ normalized total free energy, E/E_0

γ surface or interfacial energy

h film thickness

h_0 initial film thickness

i interfacial (index)

I $\gamma_i / \gamma_t + \gamma_i$

p pyramidal (index)

P $\gamma_p / \gamma_t + \gamma_i$

s substrate surface (index)

S $\gamma_s / \gamma_t + \gamma_i$

t film top surface (index)

T $\gamma_t / \gamma_t + \gamma_i$

V_0 initial film volume

y $y = \left(x - \dfrac{\sqrt{2}h_0}{\tan\alpha} \right)$

x hole-size variable ($1/2$ the diagonal of the growing hole)

x_{max} maximum hole-size at the end of a given regime

26

Appendix II: Equilibrium Crystal Shape of the Thin Film

The problem of finding the equilibrium shape of a single crystal of finite volume was first solved by Wulff.[17] In this treatment, Wulff showed that the ratio of the surface energies to distance from a common origin within the single crystal were constant, *i.e.*,

$$\gamma_1/d_1 = \gamma_2/d_2 = \gamma_3/d_3 = ... = \gamma_i/d_i = \text{constant} , \qquad \text{(A1)}$$

where γ_i is a specific facet energy (or orientation dependent surface energy) and d_i is the distance along a facet normal to the common origin. This relationship bears Wulff's name. In a *Wulff plot*, the surface energies are plotted radially as a function of orientation. The equilibrium crystal shape is then given by the locust of inner tangent planes to the γ surface[19].

Winterbottom[16] treated the problem of the equilibrium shape of a single crystal particle of finite volume on a semi-infinite single crystal substrate. In this treatment, the substrate maintains a flat interface. Further, Winterbottom included surface energy anisotropy for the single crystal particle. Winterbottom showed that the Wulff relations also hold in this case, with the modification that for all orientations corresponding to the particle interface with the substrate, the modified surface energy γ^* must be used, where

$$\gamma^* = \gamma_i - \gamma_s . \qquad \text{(A2)}$$

γ^* represents the proper energy contribution, for where the particle contacts the substrate, the appropriate energy is given by γ_i, but free substrate area is

removed, and thus γ_s must be subtracted from γ_i. Formally, since the particle is faceted, no proper wetting angle can be defined, rather changing values of $(\gamma_i\text{-}\gamma_s)$ control the aspect ratio of the particle. However, $(\gamma_i\text{-}\gamma_s)$ will be referred to as a measure of the degree of "wetting" between the film and the substrate.

Winterbottom classified the possible substrate-particle configurations into different classes: non-wetting; partial-wetting (two sub-classes); and complete wetting, as shown in the left panel of Fig. 13. The analogous behavior for liquid droplets on single crystal substrates is shown in the right panel of Fig. 13. Note that in the non-wetting case, shown in Fig. 13a, that the solid particle has a facet in contact with the substrate, and thus gives rise to the appearance of a wetting angle, whereas the liquid droplet appears to have a single point of contact with the substrate. When $0 < (\gamma_i\text{-}\gamma_s) < \gamma_t$, the inclined facet plane that intersects the film/substrate interface will form an obtuse angle with the interface as shown in Fig. 13b. Whereas when $-\gamma_t < (\gamma_i\text{-}\gamma_s) < 0$, the inclined facet plane intersecting the film/substrate will form an acute angle with the interface as shown in Fig. 13c. When $(\gamma_i\text{-}\gamma_s) < -\gamma_t$, the film completely wets the substrate, as shown in Fig. 13d.

The cases relevant for this study were normalized by γ_t and predict the following wetting behavior:

partial-wetting: $\qquad\qquad 1 > \dfrac{\gamma_s}{\gamma_t} - \dfrac{\gamma_i}{\gamma_t} \geq 0$, and $\qquad\qquad$ (A3)

complete-wetting: $\qquad\qquad \dfrac{\gamma_s}{\gamma_t} - \dfrac{\gamma_i}{\gamma_t} \geq 1$. $\qquad\qquad$ (A4)

These results concur with the experimental and theoretical observations in this study. For example in Fig. 12 complete coverage was calculated for all

$\gamma_s/\gamma_t > 1.1$ with $\gamma_i/\gamma_t > 0.1$, for all h_0/a ratios. Substituting these values into eqn. (A4), exactly fulfills Winterbottom's requirement for complete coverage. For $0.7 < \gamma_s/\gamma_t < 1.1$ in Fig. 12 partial wetting is found for a range of thicknesses, which, for small interfacial energies, also can be expected from eqn. (A3).

References

1. M.L. Gimpl, A.D. McMaster, and N. Fuschillo, "Amorphous Oxide Layers on Gold and Nickel Films Observed by Electron Microscopy," *J. Appl. Phys.*, **35** (12), 3572 (1964).

2. W.M. Cane, J.P. Spratt, and L.W. Hershinger, "Effects of Annealing on Thin Gold Films," *J. Appl. Phys.*, **37** (5), 2085 (1966).

3. R.E. Hummel, R.T. De Hoff, S. Matts-Goho, W.M. Goho, "Thermal Grooving, Thermotransport and Electrotransport in doped and undoped thin gold Films," *Thin Solid Films*, **78** (1), 1 (1981).

4. L. Bachmann, D.L. Sawyer, and B.M. Siegel, "Observations on the morphological changes in thin copper deposits during annealing and oxidation," *J. Appl. Phys.*, **36** (1), 304 (1966).

5. V. A. Mazur and M.G. Goldiner, "Low Temperature Disintegration of Thin Solid Films," *Phys. Lett. A*, **137** (5), 69 (1989).

7. N.L. Wu and J. Phillips, "Reaction-enhanced Sintering of Platinum Thin Films during Ethylene Oxidation," *J. Appl. Phys.*, **59** (3), 3572 (1986).

8. D.J. Srolovitz and S. A. Safran, "Capillary Instabilities in Thin Films. I. Energetics," *J. Appl. Phys.*, **60** (1), 247 (1986).

9. D.J. Srolovitz and S. A. Safran, "Capillary Instabilities in Thin Films. II. Kinetics," *J. Appl. Phys.*, **60** (1), 255 (1986).

10. K.T. Miller, F.F. Lange, and D.B. Marshall, "The Instability of Polycrystalline Thin Films: Experiment and Theory," *J. Mater. Res.*, **5** (1), 157 (1990).

11. A. Seifert, F.F. Lange, and J.S. Speck, "Epitaxial Growth of $PbTiO_3$ Thin Films on (001) $SrTiO_3$ from Solution Precursors," *J. Mater. Res.* **10,** (3), 680 (1995).

12. S.R. Gurkovich and J.B. Blum in *Ultrastructure Processing of Ceramics, Glasses and Composites,* edited by L.L. Hench and D.R. Ulrich, Wiley-Interscience, NY, 152 (1984).

13. C. Herring, "Some Theorems on the Free Energies of Crystal Surfaces," *Phys. Rev.*, **82** (4), 87 (1951).

14. W.W. Mullins, "Flattening of a Nearly Plane Solid Surface due to Capillarity," *J. Appl. Phys.*, **30** (1), 77 (1959).

15. D.J. Srolovitz and M.G. Goldiner, "The Thermodynamics and Kinetics of Film Agglomeration," *J. Metal*, (3), 31 (1995).

16. W.L. Winterbottom, "Equilibrium Shape of a small particle in contact with a foreign Substrate," *Acta Metall.*, **15** (2), 303 (1967).

17. G. Wulff, "Zur Frage der Geschwindigkeit des Wachstums und der Auflusung der Kristallflachen," *Z. Krist.*, **34**, 449 (1901).

18. F.F. Lange, "Epitaxial Growth in Thin Films", in *Proc. Recrystallization '92*, edited by M. Fuentes and J.G. Sevillano, Trans. Tech. Publications, Brooksfield, VT, 81 (1992).

19. C.H.P. Lupis, *Chemical Thermodynamics of Materials* (North-Holland, New York, 1983) p. 368.

Figure Captions

Figure 1   AFM image of a $PbTiO_3$ film with a standard thickness of ~120 nm. Ferroelectric a- and c-domains can be seen.

Figure 2   AFM image of an epitaxial $1/2$-standard thickness $PbTiO_3$ film with strongly faceted pores, leaving ~30% of the substrate area uncovered. An AFM section-analysis was carried out along line 'A'. The scan gives a pore-wall inclination angle of ~54°.

Figure 3   AFM image of a $PbTiO_3$ film of standard thickness (~120 nm) with a {111} faceted pit. The ferroelectric twin-planes on {101} intersect the film surface along [100] and [010].

Figure 4   AFM micrograph of an epitaxial $1/8$-standard thickness lead titanate film. The film is broken up into islands of an average height of ~60 nm. ~70% of the substrate area is exposed.

Figure 5   Series of SEM micrographs of the same area at increasing heat-treatment temperature. Large faceted pores appear to form where small pores at lower temperature form around abnormally large grains (see markers). Images are shown for the following progressively increasing heat treatment temperatures where: a. 600°C/1h; b. 650°C/1h; c. 700°C/1h; d. 750°C/1h.

Figure 6   Schematic of the configurational change of the unit cell chosen for the free energy calculation. The hole size x is varied so that pyramidal holes form at the corners of the unit cells and grow until they overlap and the film breaks up into islands.

Figure 7   Free energy dependence on the normalized hole size x/a in the first regime for $\alpha = 54.7°$ and γ_p/γ_t values of 1.73, 1.0, 0.8, 0.577, and 0.4. The change from the continuous to the dashed free energy curves marks the transition into regime 2 for a film with $h_0/a = 0.1$.

Figure 8   a) Geometric representation of the stability regimes of (111)- and (100) surfaces in a cubic system. For $\frac{1}{3}\sqrt{3} < \gamma_{111}/\gamma_{100} < \sqrt{3}$ both surfaces are stable.
            b) Schematic of a Wulff plot with stable (111) and (100) planes. The cusps define the stable surfaces and the inner tangent line of the plot gives the equilibrium crystal shape.

Figure 9   Free energy dependence on the normalized hole size x/a over all four regimes with $\gamma_p/\gamma_t = 0.8$, $\gamma_i/\gamma_t = 0.1$, $\gamma_s/\gamma_t = 1.0$, and $\alpha = 54.7°$, plotted for normalized initial film thicknesses h_0/a of 0.05, 0.038, 0.031, 0.0225, and 0.015.

Figure 10   Stability diagram mapped for varying initial film thickness h_0/a and ratio of facet to top surface energy γ_p/γ_t. The following variables are held fixed for this diagram: $\gamma_i/\gamma_t = 0.1$, $\gamma_s/\gamma_t = 1.0$, and $\alpha = 54.7°$.

Figure 11   Stability diagram mapped for varying initial film thickness h_0/a and ratio of the film/substrate interfacial energy to the top surface energy γ_i/γ_t. Different film configurations are stable depending on the initial film thickness. The following variables are held fixed for this diagram: $\gamma_p/\gamma_t = 0.8$, $\gamma_s/\gamma_t = 1.0$, and $\alpha = 54.7°$.

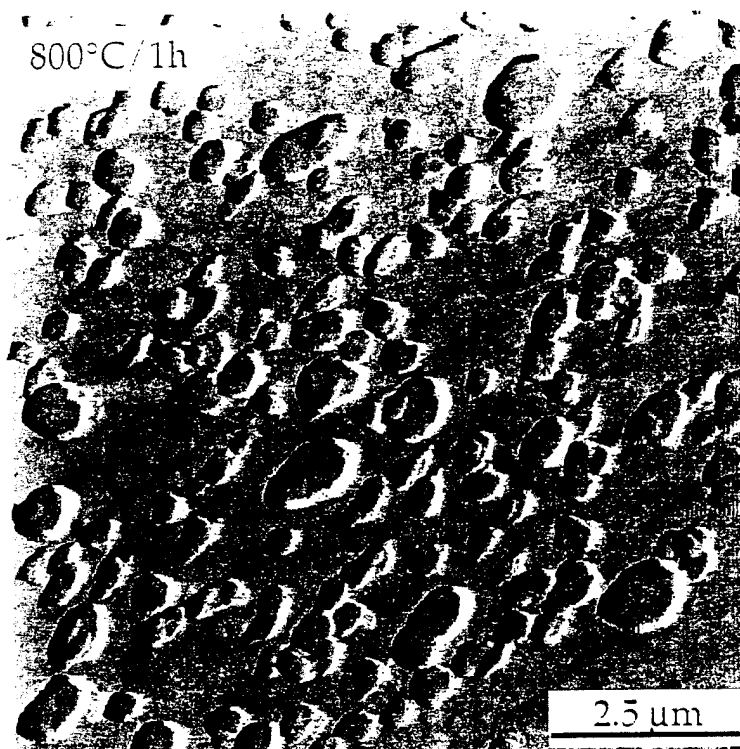Figure 12   Stability diagram mapped for varying initial film thickness h_0/a and ratio of the exposed substrate energy to top surface energy γ_s/γ_t. The following variables are held fixed for this diagram: $\gamma_p/\gamma_t = 0.8$, $\gamma_i/\gamma_t = 0.1$, and $\alpha = 54.7°$.

Figure 13   Schematic γ-plots and corresponding equilibrium shapes for a single crystal particle and a liquid droplet on a single crystal substrate: a) non-wetting, b) partial wetting $(\gamma_i - \gamma_s) > 0$, c) $(\gamma_i - \gamma_s) < 0$, and d) complete wetting (after Winterbottom[16]).
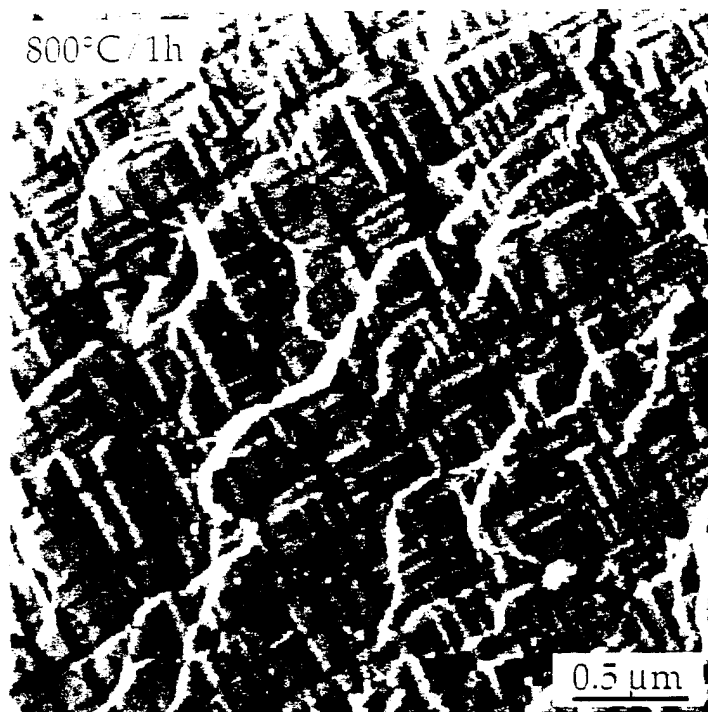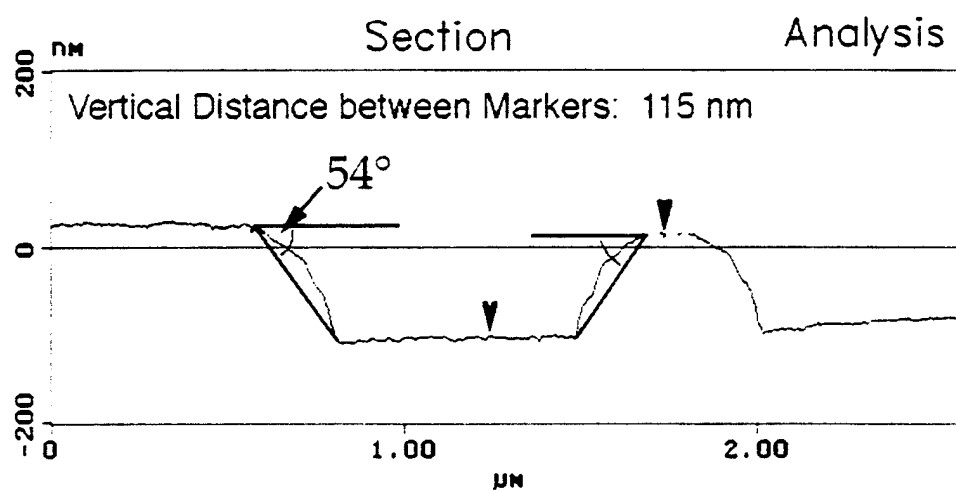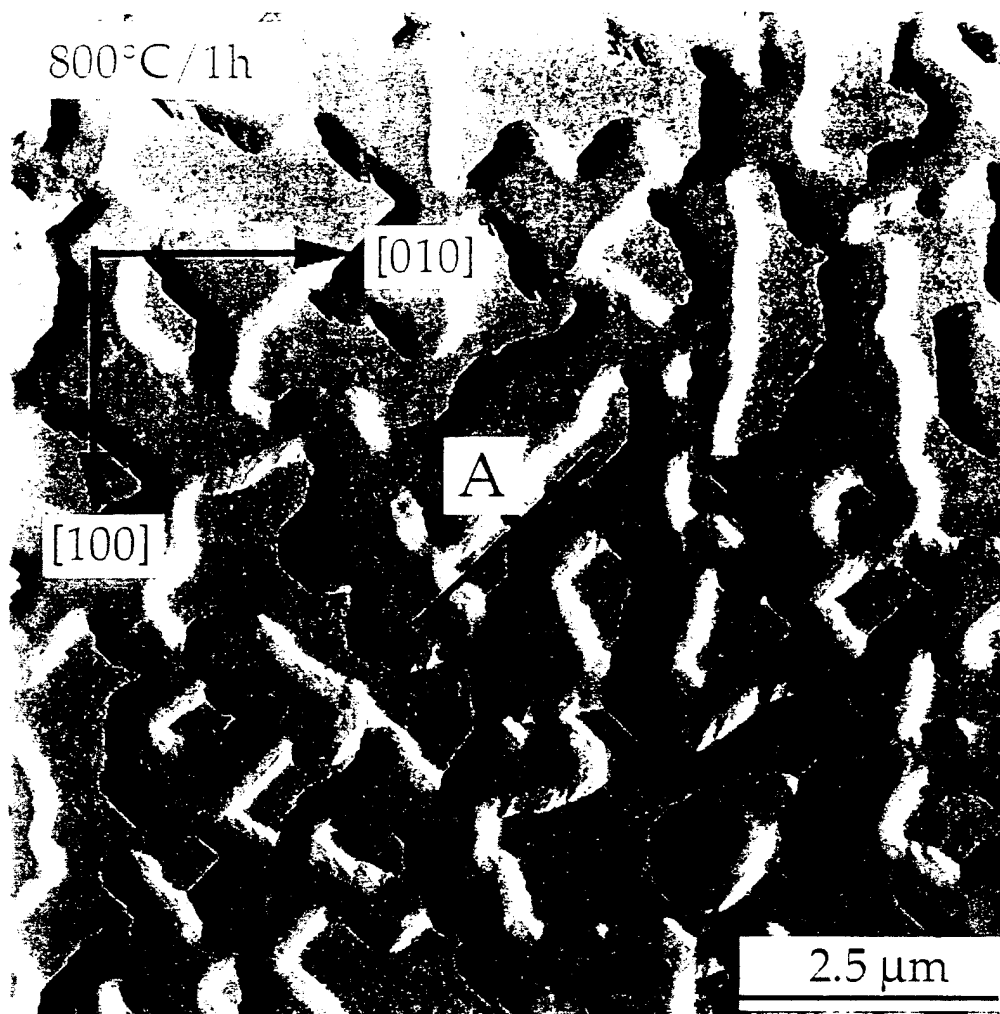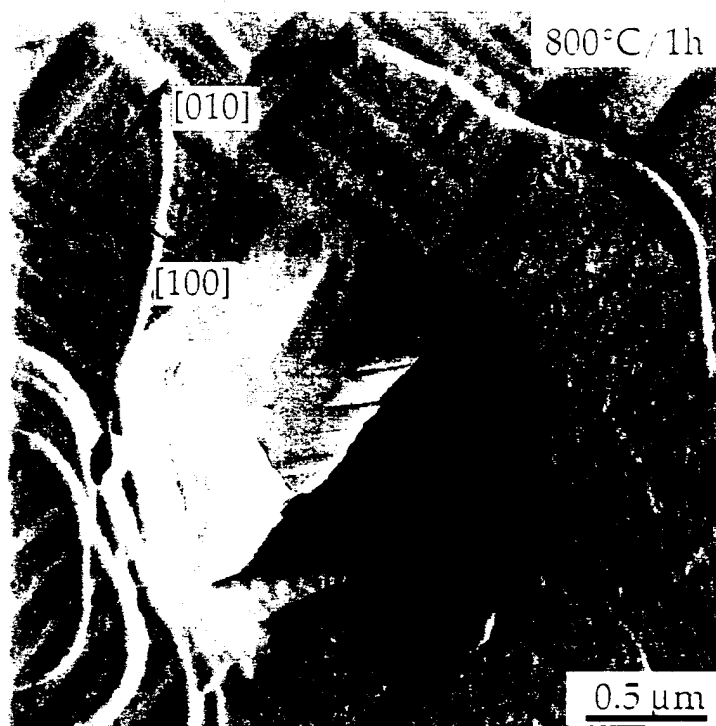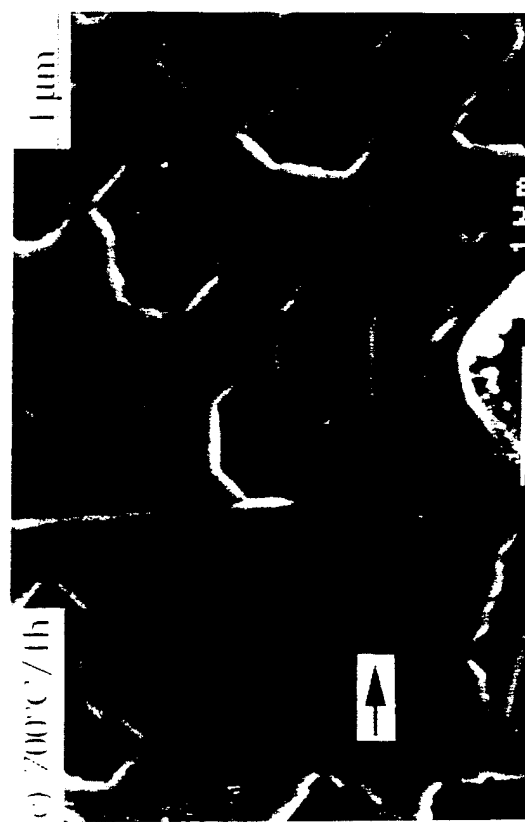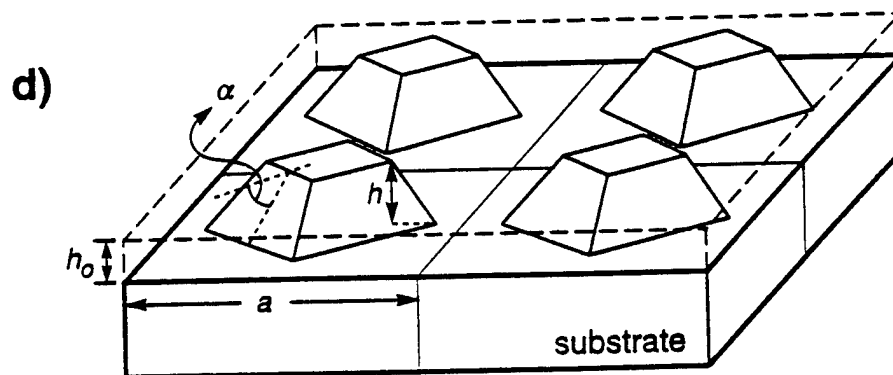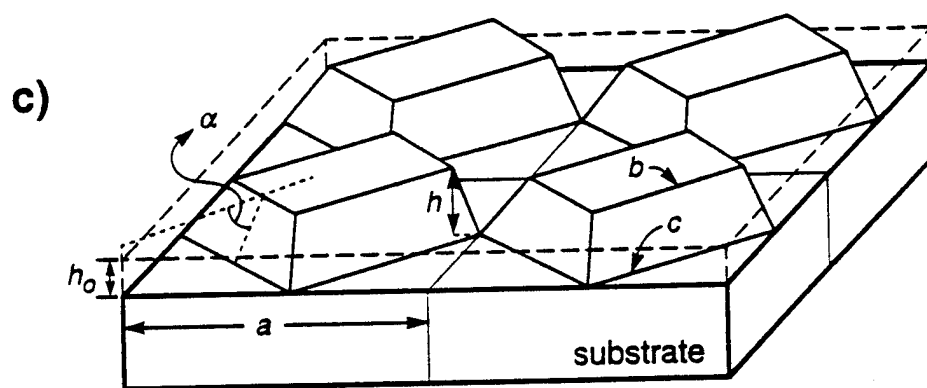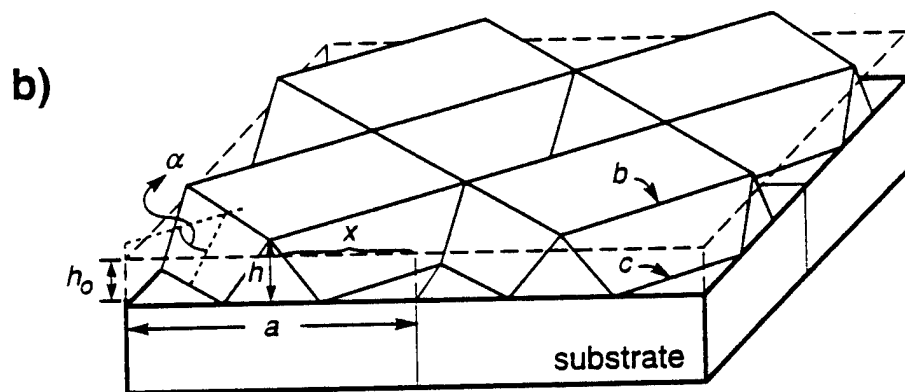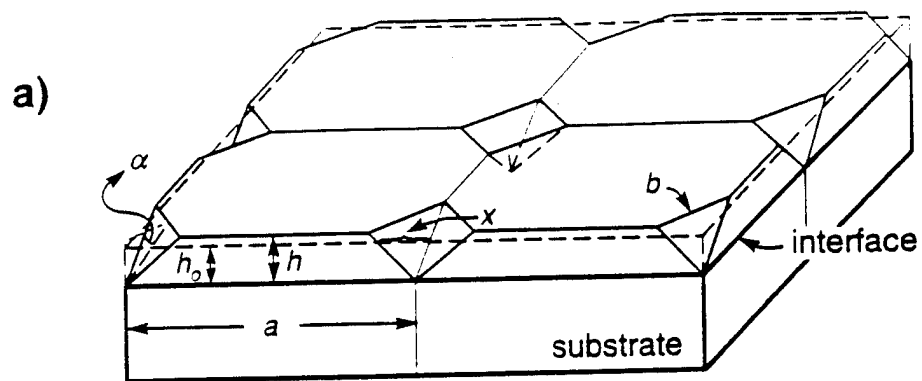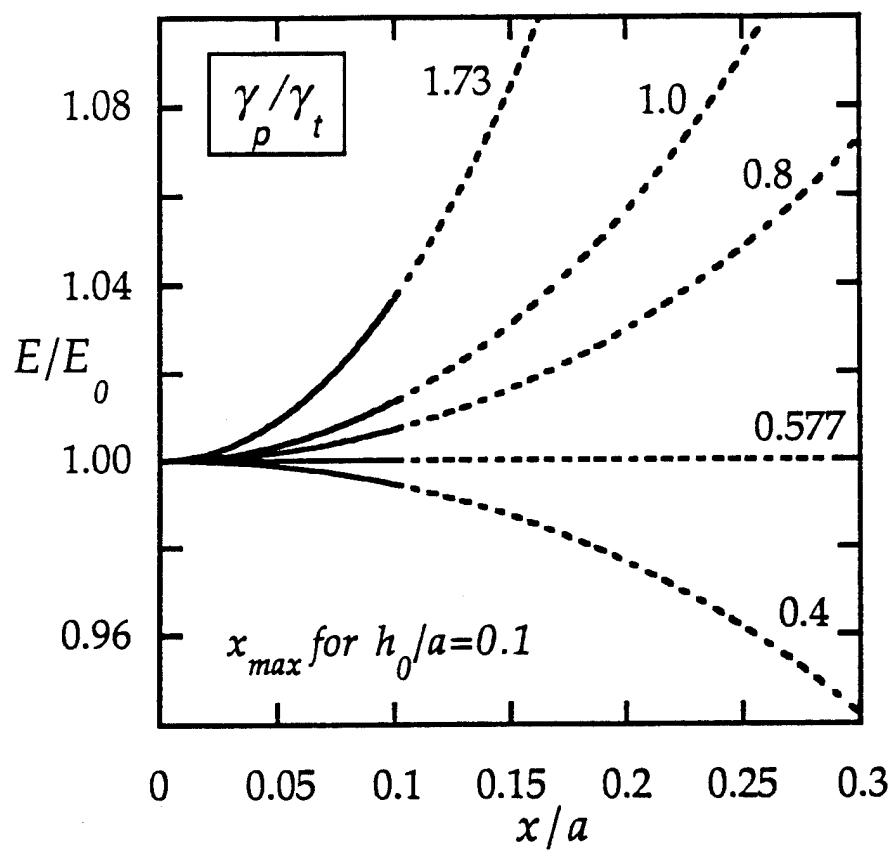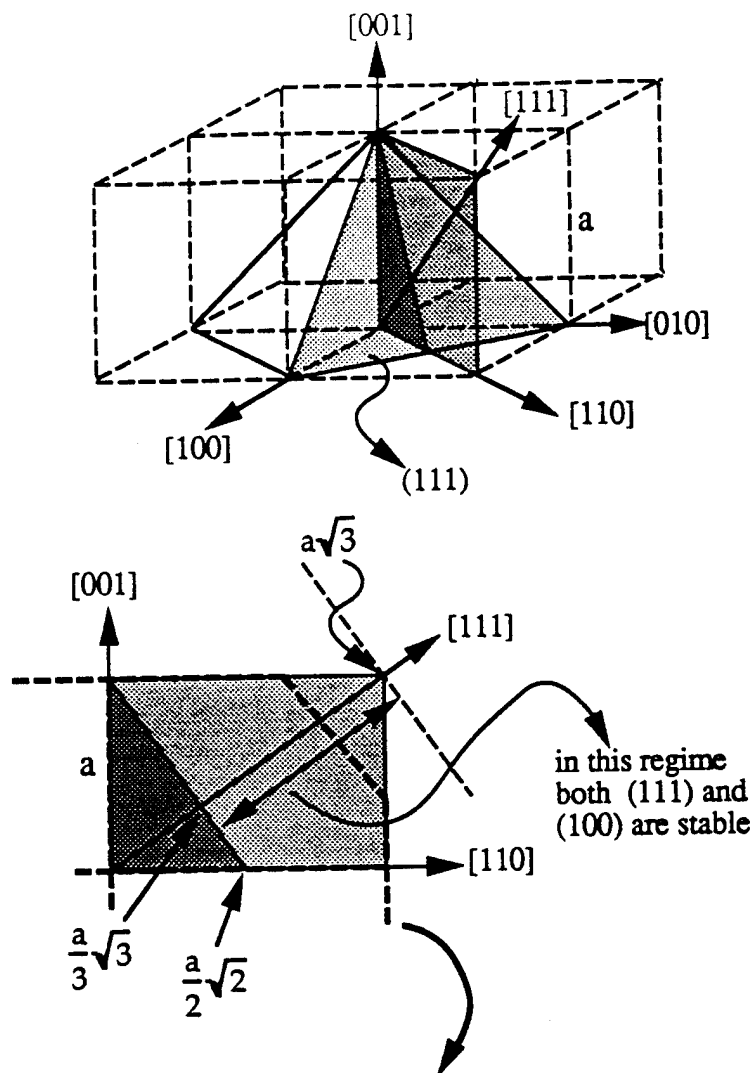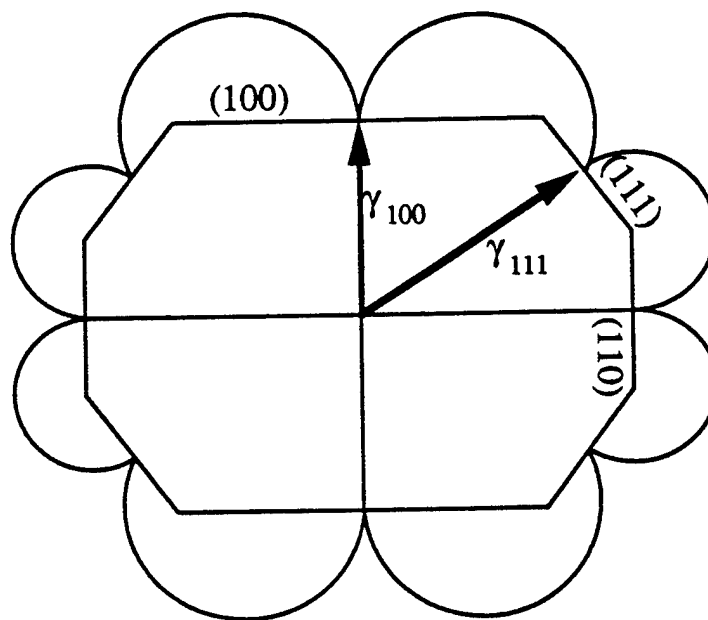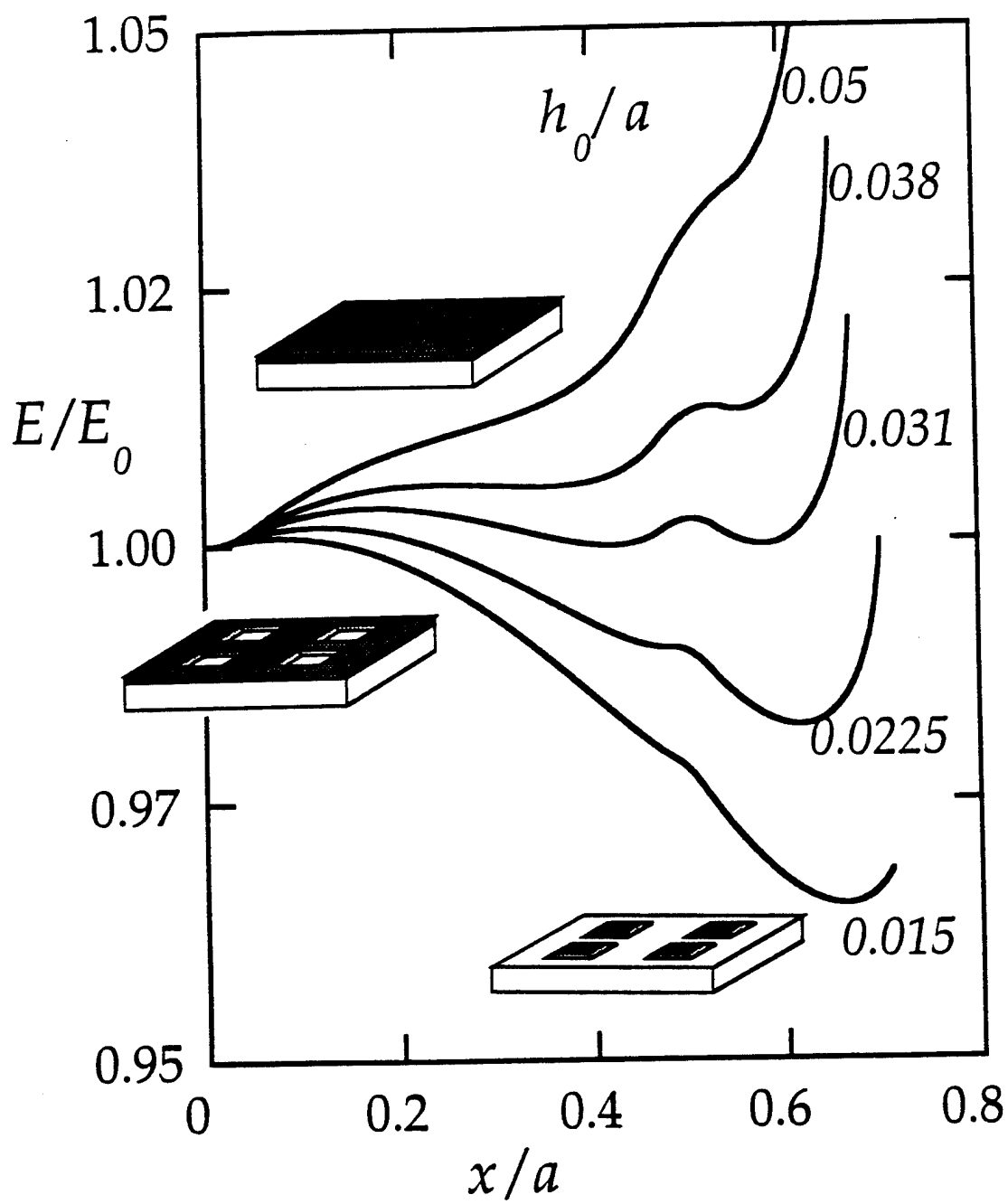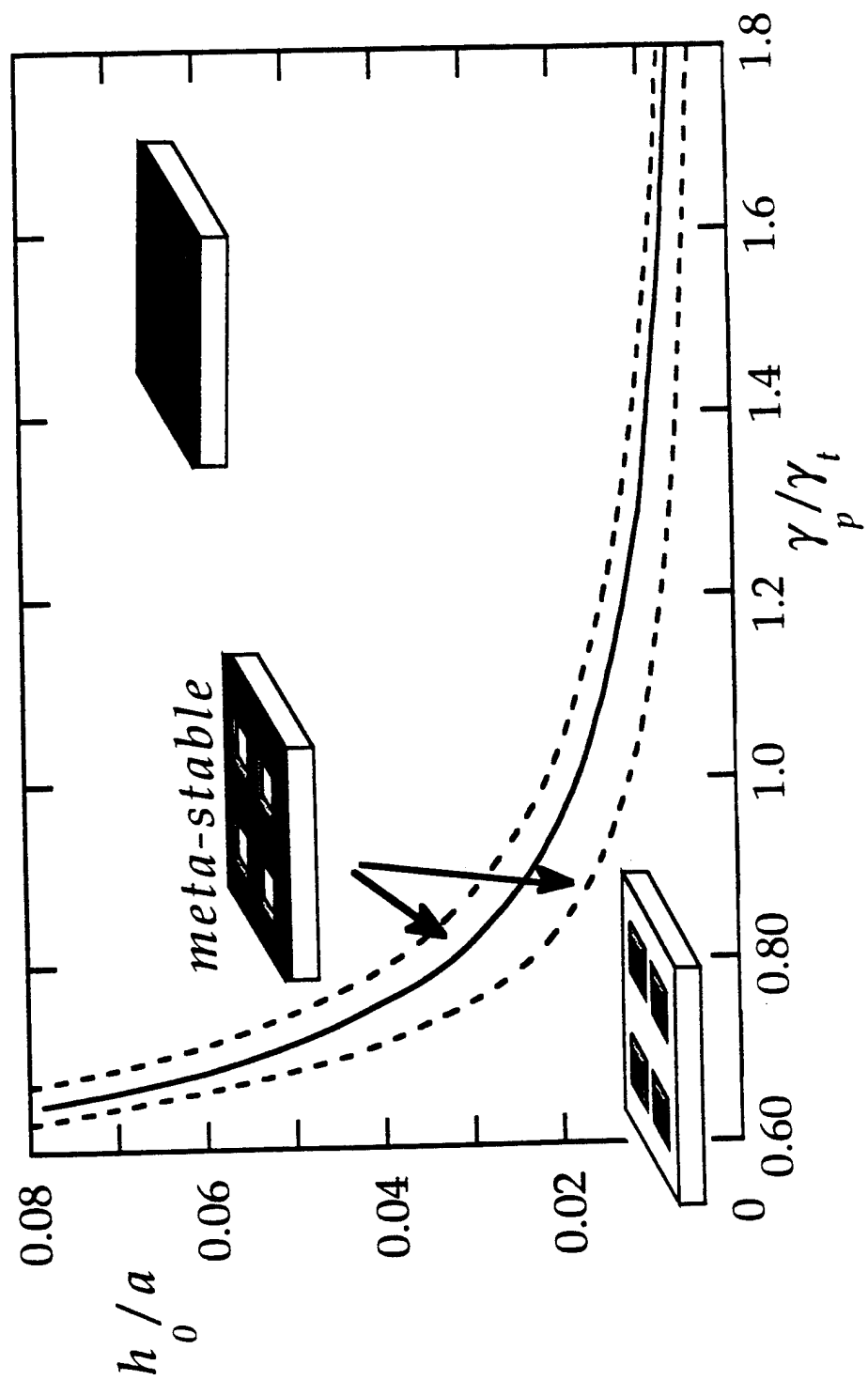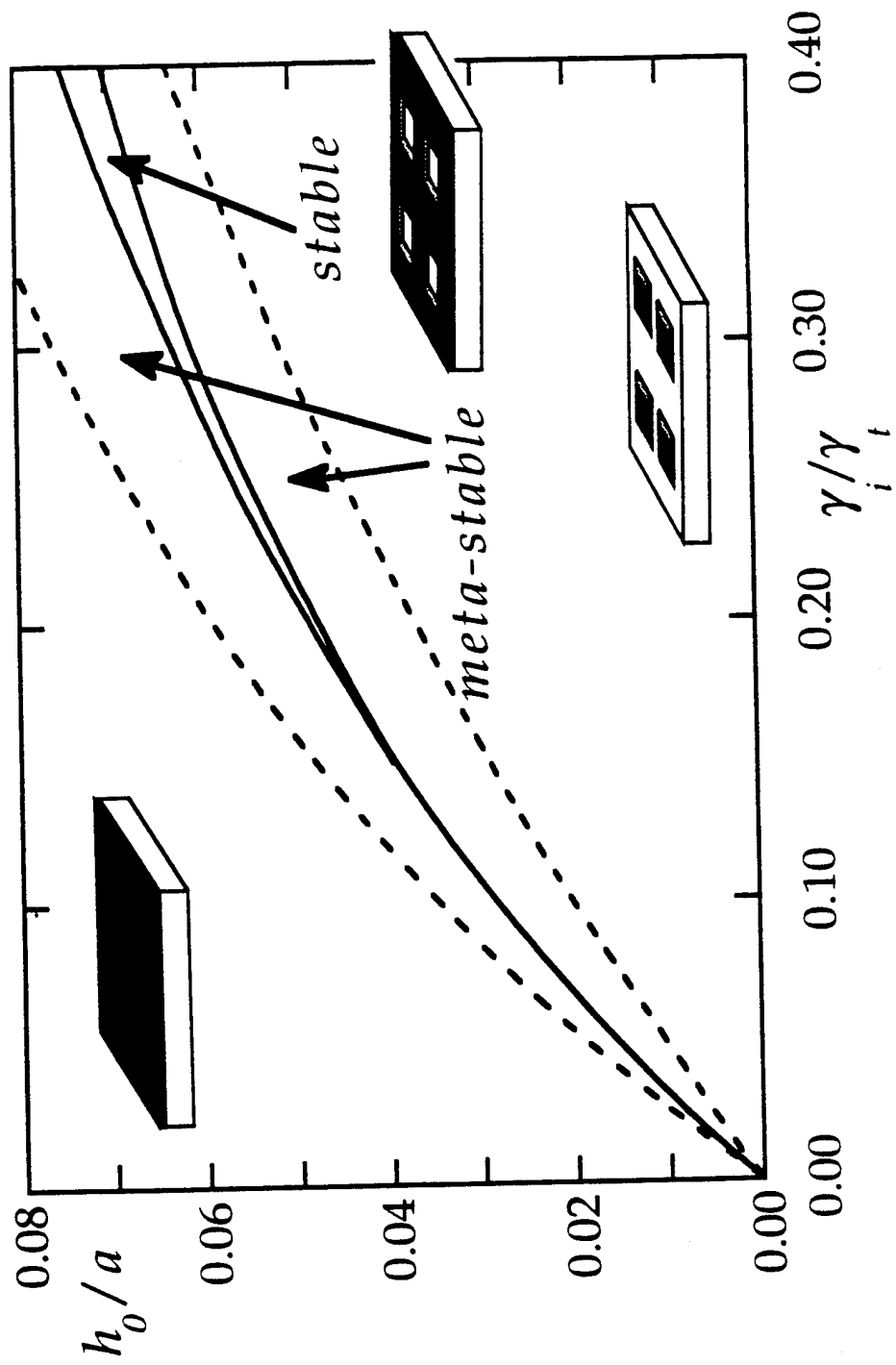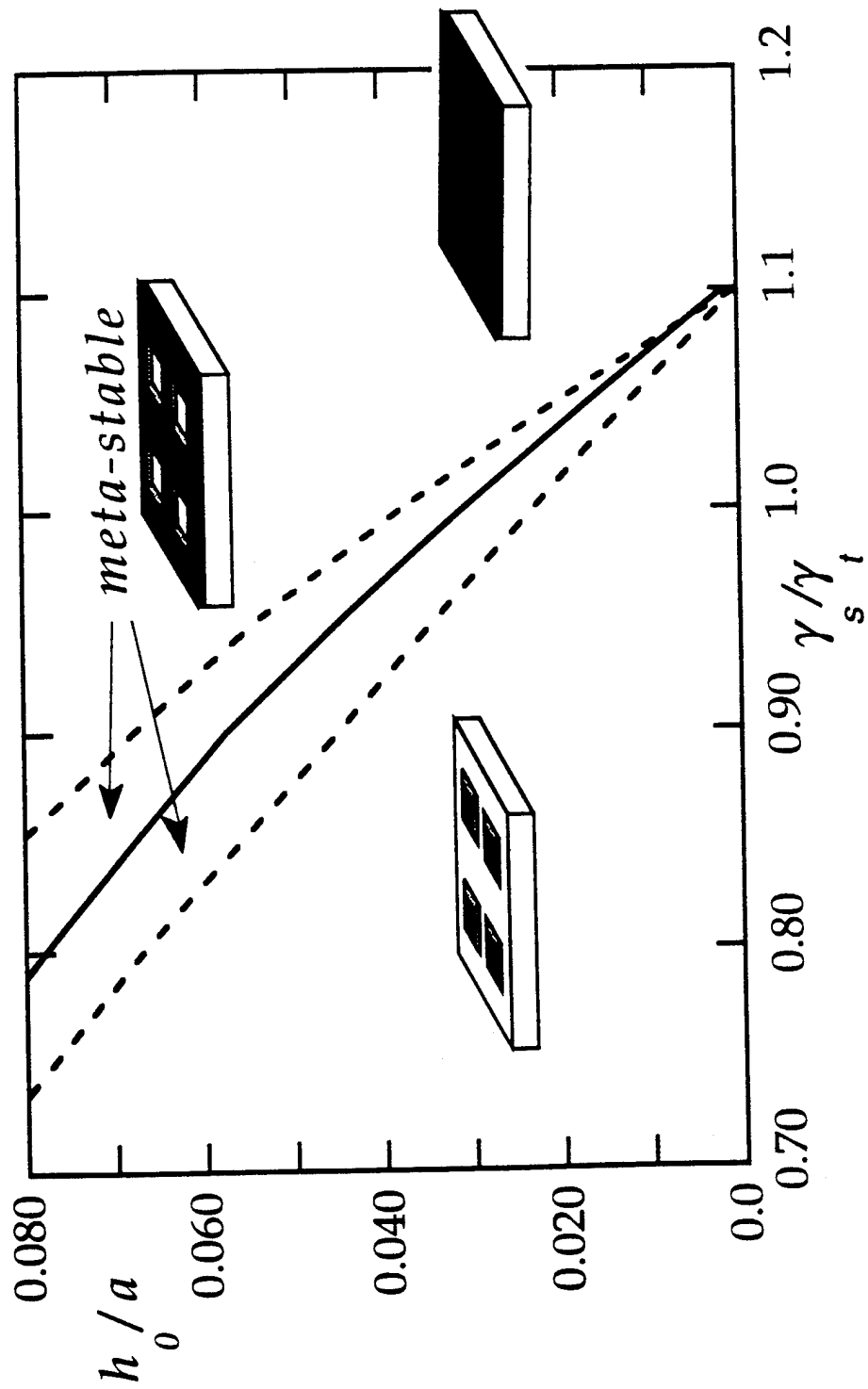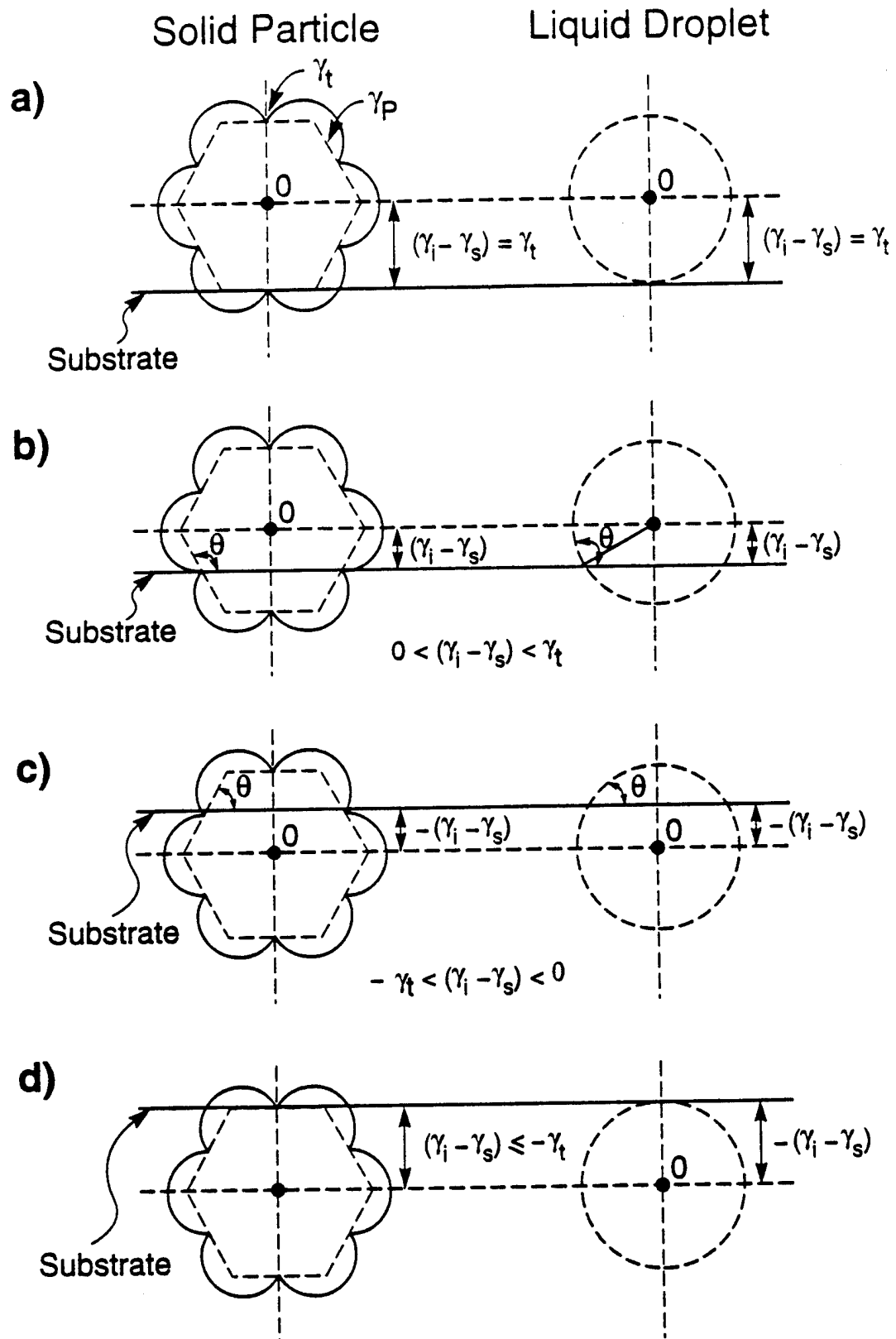
800°C / 1h

5.0 nm

0

0.5 µm

800°C/1h

[010]

[100]

A

2.5 μm

Section   Analysis

nm

200

Vertical Distance between Markers: 115 nm

54°

0

-200

0   1.00   2.00

μm

800°C/1h

[010]

[100]

5.0 nm

0

0.5 μm

800°C/1h

5.0 nm

0

2.5 um

a) 600°C/1h

b) 650°C/1h

c) 700°C/1h

d) 750°C/1h

a)
end of 1st regime

b)
end of 2nd regime

c)
end of 3rd regime

d)
end of 4th regime

FIG. 6

FIG. 7

a)

$a\sqrt{3}$

in this regime
both (111) and
(100) are stable

$\frac{a}{3}\sqrt{3}$

$\frac{a}{2}\sqrt{2}$

b)

(100)

γ_{100}

(111)

γ_{111}

(110)

FIG. 8

FIG. 9

FIG. 11

meta-stable

h_0/a

γ_s/γ_t

Fig. 12

Solid Particle   Liquid Droplet

a) $(\gamma_i - \gamma_s) = \gamma_t$ $(\gamma_i - \gamma_s) = \gamma_t$

Substrate

b) $(\gamma_i - \gamma_s)$ $(\gamma_i - \gamma_s)$

Substrate

$0 < (\gamma_i - \gamma_s) < \gamma_t$

c) $-(\gamma_i - \gamma_s)$ $-(\gamma_i - \gamma_s)$

Substrate

$-\gamma_t < (\gamma_i - \gamma_s) < 0$

d) $(\gamma_i - \gamma_s) \leq -\gamma_t$ $-(\gamma_i - \gamma_s)$

Substrate

FIG. 13

Nano-Structures via Diffusion Limited Crystallization from Solution Precursors: Synthesis and Properties

Contract AFOSR F49620-94-1-0229

Final Report

and Technical Report No. 3

period: April 15, 1994-April 14, 1995

Infiltration of Porous Alumina Bodies with Solution Precursors: Strengthening via Compositional Grading, Grain Size Control and Transformation Toughening

Paul Honeyman-Colvin* and Fred F. Lange

Materials Department
College of Engineering
University of California, Santa Barbara
Santa Barbara, CA 93106

Infiltration of Porous Alumina Bodies with Solution Precursors: Strengthening via Compositional Grading, Grain Size Control and Transformation Toughening

by

Paul Honeyman-Colvin* and Fred F. Lange

Materials Department
University of California at Santa Barbara
Santa Barbara, CA 93106

Abstract

Alumina powder compacts, partially densified with a low temperature heat treatment and then cut into bars, were infiltrated with liquid precursors that decomposed to either mullite ($3Al_2O_3 \cdot 2SiO_2$), fully stabilized zirconia (cubic-$Zr(8Y)O_2$), or partially stabilized zirconia (tetragonal-$Zr(4Y)O_2$). The specimens were repeatedly infiltrated and pyrolyzed to achieve a higher concentration of the precursor near the surface. The infiltrated bodies were then densified at 1500 °C/2 h. Residual stresses developed during cooling from the densification because of the higher concentration of the second phase near the surface. At least 10 bars of each two-phase material were fractured in 4-point bending to determine the effect of the second phase on strength. The alumina bars without a second phase had a larger grain size (≈ 7 μm) and a mean strength of 253 MPa. Both intruded phases significantly reduced the grain size to $\approx$ 1μm. Despite their higher concentration near the surface and apparent surface tensile stress, both of the $Zr(Y)O_2$ phases increased the mean strength to 413 MPa (c-$Zr(8Y)O_2$) and 582 MPa (t-$Zr(4Y)O_2$-an apparent toughening agent). The mullite second phase produced a high mean strength of 588 MPa, due apparently, to its concentration gradient and the apparent, compressive surface stress.

* Partial fulfillment for Master of Science Degree

1 Introduction

As demonstrated by others, [1-9] a second phase can be introduced into a porous ceramic by infiltration with a liquid precursor that is converted into an inorganic phase during pyrolysis(decomposition upon heating). A variety of unique microstructures (graded, multi-phase, partially porous to fully dense, etc.) with unique thermo-mechanical properties (designed residual stresses, graded elastic properties, etc.) can be envisaged when processing is performed by infiltration. In many cases, as explored here, a compositional gradient is introduced that produces residual surface stresses with the intent to increase strength. [4-7] In addition, the precursor can be used to both increase the relative density and strengthen a powder compact without shrinkage. [9] The lack of shrinkage during the strengthening of a powder is an advantage in forming ceramic composites where conventional strengthening via densification is constrained and leads to the formation of crack-like voids. [9]

As reviewed elsewhere, [10] a variety of solution chemistries exist (soluble metallorganics, salts, gel forming reactants, etc.) to synthesize multi-element inorganics. After excess solvent is removed via evaporation, a solid (or gel) precursor forms that pyrolyzes to the desired compound during a low temperature heat treatment (usually < 500 °C). Since the solid precursor decomposes to a solid inorganic and a volatile gas, a large volume decrease accompanies pyrolysis. Because pyrolysis occurs at very low temperatures relative to the compound's melting temperature, the free energy change for crystallization, ΔG_c, is large, and the critical nucleus size required for spontaneous crystallization is small. Thus, the crystallization of a connective (partially sintered) network of nano-crystallites (< 2 nm) is commonly observed; crystallization typically occurs at temperatures where long-range diffusion is kinetically limited and thus metastable phases (extended solid-solutions and non-equilibrium structures) can crystallize.

Tu and Lange [9] have pointed out two problems that can be avoided when

2

infiltrating a powder compact with a precursor. The first problem concerns the development of surface cracks caused by differential shrinkage of the precursor, relative to the elastic powder compact, during either drying or pyrolysis. Surface cracks are produced when a film of the precursor is left on the surface after infiltration. When this film shrinks during either drying or pyrolysis, Tu and Lange [9] show that some cracks that extend across the film due to constrained, differential shrinkage can also extend into the surface of the powder compact. Cracking can be avoided by either removing the film prior to crack extension or increasing the crack growth resistance of the underlying powder compact by, e.g., forming necks between the touching particles by a heat treatment prior to infiltration. The second problem concerns the concentration of precursor molecules near the surface during evaporative drying. Tu and Lange [9] show that if the precursor molecules are mobile, they move to the surface with the evaporating liquid. This problem is avoided making the precursor molecules immobile by gelling the precursor prior to drying.

Green and Marple [5] used ethyl-silicate precursor molecules in an alcohol solution to infiltrate porous, alumina bodies. Hydrolyzed, ethyl-silicate decomposes to SiO_2 at low temperatures, and reacts with the alumina at high temperatures to convert a portion of alumina body into mullite. They observed that the mullite in their experiments had a higher concentration at the surface and thus placed the surface in compression during cooling from the processing temperature. The surface compressive stresses strengthened the alumina bodies. Glass and Green [4] infiltrated partially dense ZrO_2 powder compacts with molten aluminum nitrate to produce ZrO_2/Al_2O_3 composites with a residual, compressive surface stress. They reported an increase in hardness and elastic modulus, but did not report any strengthening.

The purpose of the present work is further understand the effect of a second phase introduced via the liquid precursor route. Specifically, porous Al_2O_3 bodies were infiltrated with a liquid precursor that introduces either ZrO_2 or mullite after precursor

pyrolysis. An infiltration method was used to produce a graded composition from the surface to the interior. A higher concentration of ZrO_2 near the surface is expected to produce tensile stresses, whereas a higher surface concentration of mullite is expected to produce compressive stresses. In addition, two different ZrO_2-Y_2O_3 solid-solution compositions were used; one $(Zr(4Y)O_2)$ that produces a tetragonal phase, which is an added toughening agent to Al_2O_3, and one $(Zr(8Y)O_2)$ that produces a cubic phase that will not increase fracture toughness. As shown below the second phase inhibits grain growth, and the two phase material, regardless of the state of surface stress, had a higher strength relative to the single phase material

2 Experimental Procedure.

2.1 Preparation of Powder Compacts

An α-aluminum oxide power, (AKP-50, Sumitomo Co, Japan), was used for the current study. Its average particle diameter is 0.2 microns (Leeds-Northrup Ultrafine Particle Analyzer). Its iso-electric point was determined to be at pH 9.1. Porous alumina discs (7.5 cm in diameter and 0.5 cm thick) were prepared by pressure filtration (7 MPa) using an aqueous Al_2O_3 slurry (0.20 volume fraction) stabilized at pH 4.0. The disks were dried at room temperature for 24 hours then heated to 100°C for 12 hours were their relative density was measured to be 0.55. The specimens were strengthened in preparation for infiltration by heating to 1000 °C/1 h at 2°C/m. The relative density of the heat treated discs increased to 0.59. The disks were cut into 0.5 cm x 0.3 cm bars of different lengths. The bars were polished with 600 grit SiC paper, and their corners chamfered in preparation for flexural loading tests.

2.2 Solution Precursors, Infiltration and Densification

Precursors for both mullite and stabilized zirconia were prepared. For zirconia,

Zr-acetate [*] and yttrium nitrate [**] were dissolved in water to produce an equivalent ZrO_2 solid-solution composition containing 4 mole % Y_2O_3 to produce tetragonal $Zr(4Y)O_2$. After this precursor was formulated, it was allowed to partially evaporate until a 27% oxide yield was achieved by assay after pyrolysis. A second ZrO_2 precursor was prepared in an identical manner, except it contained 8 mole % Y_2O_3 to produce $Zr(8Y)O_2$ with a cubic structure.

A liquid precursor for mullite ($3Al_2O_3 \cdot 2SiO_2$) was made by mixing a 1:1 Si-Al double alkoxide [§] with Al(III) sec-butoxide [§§], to achieve the proper Al to Si ratio of 3:2. The solution was diluted with anhydrous butanol to lower its viscosity. A batches of hydrolyzed mullite precursor was heated to 1000°C, 1100°C, 1200°C, 1300°C, 1400°C, and 1500°C for several hours, to determine the temperature were crystalline mullite was formed by x-ray diffraction analysis (XRD)[^] .

The infiltration kinetics of the precursors were determined by suspending a partially densified alumina sample from a wire frame- attached to an electronic balance.[*] The each specimen was suspended in a liquid precursor and its weight was recorded as a function of time. After infiltration was complete, the density of each precursor was determined by weighing a know volume (100ml). Knowing the density of the precursor and the weight increase during infiltration, the infiltrated volume could be graphed as a function of time.

The partially dense powder compacts were soaked in each of the liquid precursors repeatedly for a fixed period, pre-determined to be sufficient to fully infiltrate the body during the initial infiltration cycles, but to only partially infiltrated the body for the last few infiltration cycles. The initial infiltration cycles produced a

---

[*] Zr-Acetate. Magnesium Elektron, Flemington NJ
[**] yttrium nitrate, Aldrich Chemical Company, Inc., Milwaukee, WI
[§] Si-Al Double Alkoxide, Gelest Inc., Tullytown, PA
[§§] Al(III) sec-butoxide, Johnson-Mathey, Inc., Milwaukee, WI
[^] Scintag model 6300, Santa Clara CA
[*] Mettler model AE 163, Hightstown, NJ

5

uniform distribution of the second phase [9], whereas the latter infiltration cycles produce a greater concentration of the second phase near the surface. Each cycle comprised of infiltration by soaking, gelling, and pyrolysis at 850°C for 1 h. In all cases, the bars were infiltrated with 10 cycles, soaking for 4 hours each cycle. The air entrapped within the bars was not evacuated prior to infiltration. After each infiltration, the bars were soaked in an appropriate gelling agent for 3 h to gel the precursor and immobilize the precursor molecules [9]. Ammonium hydroxide (15M) was used to gel the Zr-acetate precursor solution. The Al(III) sec-butoxide, and Si-Al double alkoxide were gelled in a dilute solution of ammonium hydroxide (0.1M). Because of the extreme moisture sensitivity of the alkoxide precursors, infiltration with the mullite precursor was carried out in a dry box, with an inert, argon atmosphere.

After infiltration was complete, the bars were heated to 1500 °C/2 h to densify the two phase materials. Alumina bars, which were not infiltrated, were also densified at the same temperature.

2.3 Strength Measurements and Characterization

The strength of all bar specimens was determined in four-point bending (inner and outer spans of 5.0 cm and 2.0 cm, respectively). These tests were performed [t] using a 100 Kg load cell and a loading rate of 0.002 in/m.

After densification, bar specimens were sectioned by diamond cutting and polishing to measure the atomic ratio, either Zr/Al or Si/Al, from the surface to the center using electron dispersive spectroscopy (EDS)[tt] within a scanning electron microscope (SEM).[ttt] A series of two-phase materials were prepared with powder mixtures of ZrO_2[¥] /Al_2O_3 and Mullite[¥¥] /Al_2O_3 and densified at 1500 °C/2h. Each two-

---

[t] Instron Model 1123, Canton, Ma
[tt] Nortran Micro-q System, Tracor-Northern, Middleton, WI
[ttt] JEOL model 6300FE, Tokyo, Japan
[¥] Zirconia TZ-8Y, TOSOH Inc., Tokyo, Japan
[¥¥] Mullite MU-107, Besterfeld U.S. Inc, NY, Ny.

6

phase material was diamond cut and polished and used as EDS standards to convert the atomic ratio obtained via EDS into volume fraction of either ZrO_2 or mullite within the Al_2O_3 bodies.   SEM micrographs were used to determine the average grain size using the linear intercept method. The relative densities of the pure alumina bars were determined by measuring dimensions and weight. For the infiltrated, two-phase materials, the weight of the infiltrated material was determined by subtracting the initial weight of the alumina body, measure prior to any infiltration, from the final weight after infiltration. The theoretical, relative density of each two phase materials was determined by calculating the volume of the second phase using its density (ρ_{Al2O3} = 3.98 g/cc, $\rho_{Zr(Y)O2}$ = 6.02g/cc, and $\rho_{mullite}$ = 3.18 g/cc) and its weight determined after cyclic infiltration.

3 Results

3.1 Infiltration

The infiltration kinetics for each of the precursors was determined by taking data for weight gain vs. time during infiltration. The data was changed to relative volume infiltrated vs. $t^{1/2}$, and plotted for the first and fourth infiltration cycle in Figs. 1 and 2, for the $Zr(4Y)O_2$ and mullite precursors, respectively.   Data for the first infiltration exhibits two distinct parabolic (linear with $t^{1/2}$) regimes. In the first regime, more rapid infiltration occurs by the flow of the liquid precursor into the porous compact. As reported elsewhere, [9] the first regime ends when the pressure of the entrapped gas becomes equal to the capillary pressure that causes fluid flow. In the second regime, the slower kinetics are governed by the diffuse of air, at higher pressure, through the liquid to the ambient, room pressure. As observed in both Figs. 1 and 2, the kinetics for the 4th infiltration is no longer parabolic. As previously reported [9], the more complex infiltration kinetics observed in subsequent cycles is caused by the filling of void space within the initial body with partially dense, second phase material

produced by previous infiltration/pyrolysis cycles. Figure 3 shows data for the relative amount of pore volume remaining after each infiltration/pyrolysis cycle, for the same specimen used to obtain the data in Figs. 1. After 4 or 5 infiltration cycles, the volume of precursor added per infiltration cycle noticeably decreases.

3.2 Characterization

As shown in Table 1, the average grain size for the single phase alumina was ≈ 7 μm, whereas the average size of the alumina grains in all of the two phase materials produced by cyclic infiltration was ≈ 1μm. Table 1 also lists the average, relative densities for each material.

Figures 4, 5 and 6 illustrate the EDS results for the volume fraction of second phase vs. the normalized distance from the sample surface, for sectioned bars containing c-$Zr(Y)O_2$, t-$Zr(Y)O_2$, and mullite second phases, respectively. Figure 7 is a SEM of a fracture surface showing that the second phase (in this case, $Zr(4Y)O_2$) is a continuous polycrystalline phase within the continuous, polycrystalline Al_2O_3 material. The other two phase materials appeared similar.

3.3 Strength Measurements

Table 1 reports the mean strength, number of specimens measured [brackets] and the Weibull modulus of the bars infiltrated with zirconia and mullite precursors, as well as the single phase, alumina bars. A $\ln\ln(N+1/N+1-n)$ vs. $\ln$(strength) plot was used to obtain the Weibull moduli (m), where N is the number of specimens, listed in increasing order strength, and n is the nth specimen in the list.

The single phase alumina bars had the lowest strength, with values between 218 MPa and 282 MPa (m = 13). The next lowest strength material contained the fully stabilized zirconia phase, c-$Zr(8Y)O_2$ with strengths between 385 and 482 MPa (m = 12). Specimens containing the tetragonal-$Zr(4Y)O_2$ second phase failed between 498 and 646

MPa (m = 12). The strongest material containing the mullite, with strengths between 528 MPa and 667 MPa (m = 14). Note that the Weibull modulus of all four materials is nearly the same (12 ≤ m ≤ 14) suggesting that the same flaw population(s) control the strength of all four materials because they were manufactured from nearly identical, partially densified powder discs.

4 Discussion

The strength results presented here indicate that at least three different phenomena for strengthening alumina were observed by introducing a second phase through a solution precursor route. These phenomena include controlling grain size, increasing the fracture toughness, and creating a compressive, surface stress.

The EDS data for the second phase in materials containing c-Zr(8Y)O$_2$, t-Zr(4Y)O$_2$, and mullite all showed a higher concentration of the second phase at the surface, decreasing to a constant value at the center of the body. Moreover, all of the concentration gradients are quantitatively similar. The surface of the two materials containing the zirconia second phase had ≈ 10 % more Zr(Y)O$_2$ at the surface relative to the center; for the other material, the surface contained ≈ 15 % more mullite than the center.

For the given densification conditions, the introduction of either zirconia or mullite as a second phase effectively reduced the alumina grain size by an order of magnitude as previously reported for two phase materials produce by a mixed powder route. [11] The effect of grain size reduction on strength appeared more significant than the concurrent production of tensile, surface stresses caused by a higher concentration of zirconia at the surface. Although the tensile stress was not measured, judging its gradient, a tensile surface stresses must exist. [6] The material infiltrated with c-Zr(8Y)O$_2$, which does not produce transformation toughening, had a mean strength of 413 MPa despite the presence of apparent tensile surface stresses. This mean value is ≈

60 % greater than the mean strength of the single phase alumina material. The use of a second phase to reduce grain size and its effect on increasing strength has been previously demonstrated by Lange and Claussen [12] for the SiC inclusions in Al_2O_3 and Green [13] for the case of ZrO_2 inclusions in $\beta"$-Al_2O_3. These authors show that the significant reduction in grain size does not lead to an increase in the critical stress intensity factor commensurate with the strength increase. Thus, as previously demonstrated and shown here as well, reducing the gain size reduces one of the major populations, viz., large grains.

Tetragonal ZrO_2 is a recognized toughening agent for alumina. [14, 15] The strength of the material containing this toughening agent. Strengthening with the t-$Zr(4Y)O_2$ second phase indicate that it increased the fracture toughness of the alumina material, as expected. By substituting the t-$Zr(4Y)O_2$ phase for the c-$Zr(8Y)O_2$, the mean strength increased from 413 MPa to 584 MPa ($\approx$ 40 %). Both the alumina materials containing the c-$Zr(8Y)O_2$ and the t-$Zr(4Y)O_2$ second phases had approximately the same grain size and approximately the same compositional gradient. It appears that the combination of grain size reduction and transformation toughening yielded more than twice the mean fracture strength of the single phase alumina material.

The mean fracture strength of the mullite infiltrated samples is the highest of all the four materials, at 588 MPa. This higher strength can not only be due to a smaller grain size, but must also be related to the compressive stresses at the surface of the material. The EDS results indicate that the mullite infiltrated samples had a similar concentration gradient to the zirconia infiltrated samples. However due to the much greater difference in CTE between alumina and mullite, the residual surface stresses were probably much greater than the zirconia case, and compressive instead of tensile.

5 Conclusions

Using a previously developed method of forming graded two-phase composites

by infiltrating partially dense alumina compacts, it was shown that a second phase could be introduced to significantly increase the mean strength of the two phase material relative to the single phase material. Three phenomena cause the higher strengths: a) All second phases, regardless of the apparent state of surface stress, substantially decrease the grain size of the alumina phase to decrease one strength controlling flaw population, viz., large Al_2O_3 grains. b) A tetragonal $Zr(4Y)O_2$ second phase was introduced which would increase the critical stress intensity factor of the composite relative to the single phase. c) Mullite, with a lower thermal expansion coefficient and with a higher concentration near the surface, places the composite's surface in compression during cooling from the processing temperature. Two of these strengthening phenomena more than doubled the mean strength of the single phase Al_2O_3 material.

Acknowledgments

References

[1]   S. Yajima, T. Shishido, and K. Okamura, "SiC Bodies Sintered with Three-Dimension Cross-Linked Polycarbosilane," Am. Ceram. Soc. Bull., [56] 12, 1060-1063 (1977).

[2]   K.S. Mazdiyasni, R. West, and L.D. David, "Characterization of Organosilicon Infiltrated Porous Reaction-Sintered Si3N4," J. Am. Ceram. Soc., 61[11-12] 504-508 (1978).

[3]   B.E. Walker, Jr., R.W. Rice, P.F. Becker, B.A. Bender, and W.S. Coblenz, "Preparation and Properties of Monolithic and Composite Ceramics Produced by Polymer Pyrolysis," Am. Ceram. Soc. Bull., 62, [8] 916-23 (1983).

[4]   S. J. Glass and D. J. Green, "Surface Modification of Ceramics by Partial Infiltration," Adv. Ceram. Mater., 2 [2] 129-131 (1987).

[5]   B. R. Marple and D. J. Green, "Incorporation of Mullite as a Second Phase into

Alumina by an Infiltration Technique," J. Am. Ceram. Soc., 71[11]C-471-C-473 (1988).

[6]   B. R. Marple and D. J. Green, "Mullite/Alumina Particulate Composites by Infiltration Processing," *J. Am. Ceram. Soc.*, **72** [11] 2043-48 (1989); II Infiltration and Characterization", **73** [12] 3611-16 (1990); III, Mechanical Properties," **74** [10] 2453-59(1991); IV, Residual Stress Profiles", **75** [1] 44(1992).

7]   B. R. Marple and D. J. Green "Graded Compositions and Microstructures by Infiltration Processing," *J. Mater. Sci.* , **28** 4637-43(1993).

8]   M.D. Sacks and S.D. Vora, "Preparation of SiO_2 Glass from Model Powder Compacts: III, Enhanced Densification by Sol Infiltration," J. Am. Ceram. Soc., 71 [4] 245-49 (1988).

[9]   W. C. Tu and F. F. Lange,"Liquid Precursor Infiltration Processing of Powder Compacts, I: Kinetic Studies and Microstructure Development; II: Fracture Toughness and Strength"; sent to J. Am. Ceram. Soc.

[10]   F. F. Lange, "Liquid Precursors for Ceramics: Kinetically Limited Crystallization, Spherical Particles, Fibers and Thin Films," *Chemical Processing of Advanced Materials, Chemical Processing of Advanced Materials*, Ed. by L.L. Hench and J.K. West, pp 611-26, John Wiley and Sons (1992).

[11]   F. F. Lange and M. M. Hirlinger, "Hindrance of Grain Growth in Al_2O_3 by ZrO_2 Inclusions," J Am Ceram Soc 67 [3], 164 (1984).

[12]   F F Lange and Nils Claussen, "Some Processing Requirements for Transformation Toughened Ceramics," Ultrastructure Processing of Ceramics, Glasses and Composites, ed by L L Hench and D R Ulrich, p 493, John Wiley (1984).

[13]   D. J. Green, "Transformation Toughening and Grain Size Control in β"-Al_2O_3/ZrO_2 Composites," J. Mat. Sci. 20 2639-46 (1985).

[14]   N. Claussen, "Fracture Toughness of Al2O3 with an Unstablized ZrO2 Dispersed Phase," J. Am. Ceram. Soc. 59 [1-2] 49-51 (1976).

[15]   F. F. Lange, "Transformation Toughening, Parts I through V," J. Mat. Sci. 17 [1] 225-63 (1982).

Table 1. Tabulated Material Properties

Material	Relative Density	Grain Size (μm)	Weibull Modulus	Mean Strength* (MPa)
Alumina	0.96	7.1	13.1	253 [10]
Alunina/Zr(8Y)O$_2$	0.98	1.2	12.1	413 [10]
Alunina/Zr(4Y)O$_2$	0.99	1.2	11.8	582 [12]
Alunina/Mullite	0.97	1.6	14.0	588 [10]

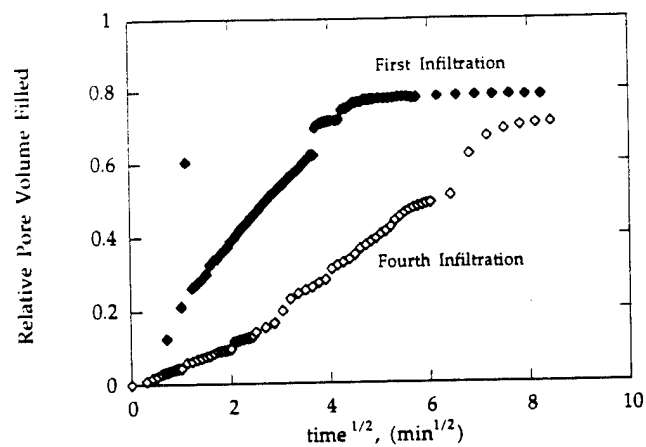* Numbers in brackets = number of specimens fractured

Figure Captions

Figure 1 First and fourth infiltration cycle reported as relative pore volume filled as a function of time$^{1/2}$ for the case of $Zr(4Y)O_2$ precursor infiltration into a porous, alumina powder compact.
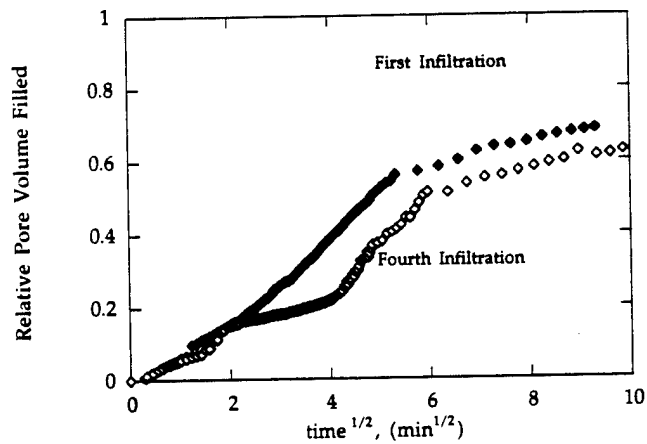
Figure 2 First and fourth infiltration cycle reported as relative pore volume filled as a function of time$^{1/2}$ for the case of Mullite precursor infiltration into a porous, alumina powder compact.
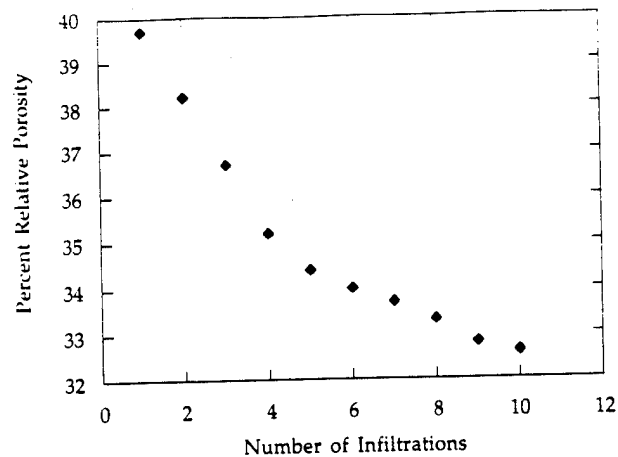
Figure 3 Relative pore volume remaining as a function of number of infiltration/ pyrolysis cycles, prior to densification for infiltration of $Zr(4Y)O_2$ precursor infiltration into a porous, alumina powder compact.
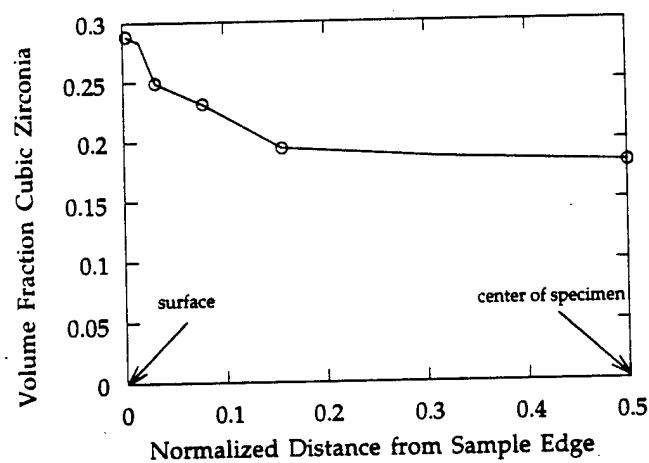
Figure 4 Concentration gradient of cubic-zirconia as a function of normalized distance from the specimen surface. Gradient recorded for specimen after densification for 1500°C/2h.

Figure 5 Concentration gradient of tetragonal zirconia as a function of normalized distance from the specimen surface. Gradient recorded for specimen after densification at 1500 °C/2h.

Figure 6 Concentration gradient of mullite as a function of normalized distance from the specimen surface. Gradient recorded for specimen after densification at 1500 °C/2h.

Figure 7 SEM micrograph of fracture surface of alumina body containing tetragonal zirconia second phase.

Figure 1   First and fourth infiltration cycle reported as relative pore volume filled as a function of time$^{1/2}$ for the case of $Zr(4Y)O_2$ precursor infiltration into a porous, alumina powder compact.

Figure 2   First and fourth infiltration cycle reported as relative pore volume filled as a function of time$^{1/2}$ for the case of Mullite precursor infiltration into a porous, alumina powder compact.

15

Figure 3   Relative pore volume remaining as a function of number of infiltration/ pyrolysis cycles, prior to densification for infiltration of Zr(4Y)O$_2$ precursor infiltration into a porous, alumina powder compact.

Figure 4   Concentration gradient of cubic-zirconia as a function of normalized distance from the specimen surface. Gradient recorded for specimen after densification for 1500°C/2h.
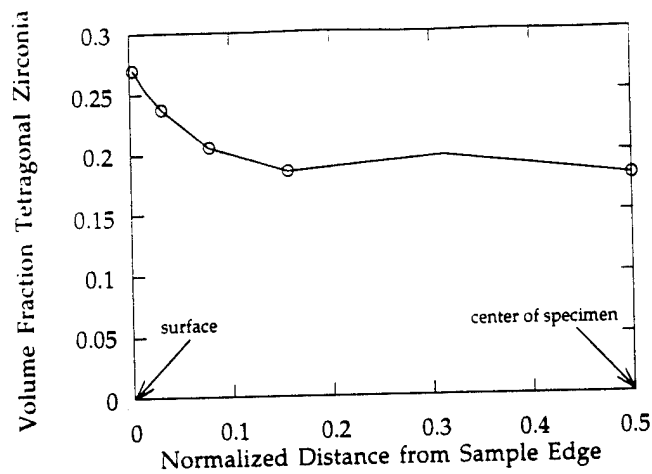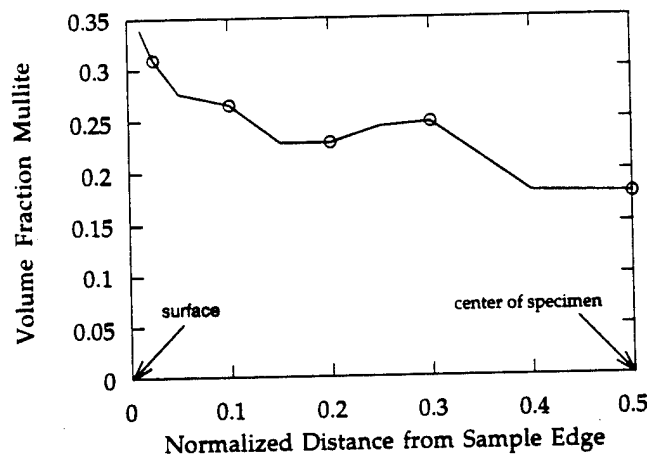
16

Figure 5   Concentration gradient of tetragonal zirconia as a function of normalized distance from the specimen surface. Gradient recorded for specimen after densification for 2 hours at 1500°C.

Figure 6   Concentration gradient of mullite as a function of normalized distance from the specimen surface. Gradient recorded for specimen after densification for 2 hours at 1500°C.
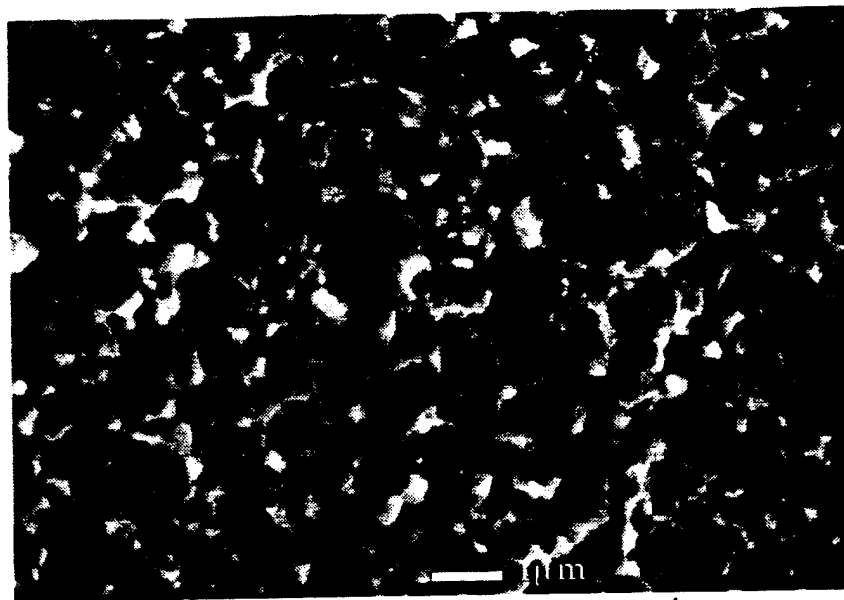
17

Figure 7   SEM micrograph of fracture surface of alumina body containing tetragonal zirconia second phase

Nano-Structures via Diffusion Limited Crystallization from Solution Precursors: Synthesis and Properties

Contract AFOSR F49620-94-1-0229

Final Report

and Technical Report No. 4

period: April 15, 1994-April 14, 1995

Pyrolysis of Pb(Zr$_{0.5}$Ti$_{0.5}$)O$_3$ Precursors: Avoiding Pb Partitioning During Pyrolysis

A.D. Polli and F.F. Lange

Materials Department
College of Engineering
University of California, Santa Barbara
Santa Barbara, CA 93106

Pyrolysis of $Pb(Zr_{0.5}Ti_{0.5})O_3$ Precursors: Avoiding Pb Partitioning During Pyrolysis

A.D. Polli and F.F. Lange

Materials Department
University of California
Santa Barbara, CA 93106

Abstract

Three different chemical precursor routes were investigated to synthesize $Pb(Zr_{0.5}Ti_{0.5})O_3$: mixing hexanoates, acetate complexing of alkoxides and the synthesis of a mixed alkoxide by the reaction of Ti- and Zr-alkoxide with Pb-acetate. For each, elemental Pb and PbO were the first crystalline phase observed during pyrolysis conditions that involved rapid heating (e.g. to 400 °C). The formation of Pb (and PbO) could be avoided by first heat treating hydrolyzed, mixed alkoxide precursor powders at 300°C for 1hour. This treatment was not effective for the two other precursors. It is concluded that both the carbonaceous content of the precursor (lowest for the hydrolyzed, mixed alkoxides) and the rate of hydrocarbon release during pyrolysis is critical to avoid the formation of elemental Pb during pyrolysis.

1. Introduction

The processing of high quality $Pb(Zr_x,Ti_{1-x})O_3$ thin films has been the focus of much research. Several commonly used precursor routes have emerged and with them, the development of different microstructures and related properties. Much work has concentrated on identifying the reasons why different precursor chemistries and processing procedures produce different microstructures and properties. For example, Lakeman and Payne [1] have shown how precursor solution processing effects the chemistry of the solution, which in turn helps determine the properties of the final film. Assink and Schwartz [2] have used ^{1}H and ^{13}C NMR to characterize solvent and ligand effects within their acetic acid solvent processes. Also, Tuttle et al.[3] have investigated the effect of the substrate on preferred orientation and remnant polarization and relative dielectric constant.

Although many precursor chemistries have been used to synthesize PZT, perhaps three chemical routes are most commonly reported. Blum and Gurkovich [4] have pioneered the use of an alkoxide-based process using titanium isopropoxide, zirconium isopropoxide, and lead(II) acetate trihydrate dissolved in 2-methoxyethanol, which can be hydrolyzed to form a gel. The chemistry of this precursor system has been characterized by Budd et al.[5] Schwartz et al.[6] have employed an approach adopted from Yi et al.[7] where titanium isopropoxide and zirconium butoxide are dissolved in acetic acid. The acetic acid acts as a chemical modifier by promoting a ligand exchange between the alcohol groups of the alkoxides and the acetate groups of the solvent, resulting in a relatively moisture

insensitive precursor. After additions of lead (IV) acetate, methanol, and water, PZT films are spun, dried, and fired. Vest and Zhu [8] have described a metallo-organic deposition (MOD) process using lead(II) 2-ethylhexanoate, zirconium 4-neodecanoate, and titanium 2-methyoxy-di-neodecanoate which they dissolved in a common solvent, xylene. After solvent evaporation, the precursor has the texture of a soap.

This research was initiated as part of a larger study concerning the crystallization of different PZT compositions within the $PbO-ZrO_2-TiO_2$ system with the goal to identify the first crystalline phase produced either during or after precursor decomposition (pyrolysis). In such studies, a precursor chemistry and procedure must be selected that avoids elemental partitioning prior to crystallization. One of our concerns was the partitioning of Pb, as an element, during the pyrolysis of precursors containing carbon. As pointed out by Mantese et al., [9] metal-organic compounds of Pb can be heated within an oxygen partial pressure 'window' that allows the synthesis of elemental Pb instead of one of its oxides. That is, Pb, and a few other metals such as Cu, Bi, etc., can exist as a native element at an oxygen partial pressure needed to 'cleave off' the hydrocarbons of the metal organic molecule. Thus, prior to our study of the diffusion limited crystallization of PZT compositions, a precursor chemistry and preparation methodology had to be identified that precluded the partitioning of elemental Pb during pyrolysis. The composition $Pb(Zr_{0.5}Ti_{0.5})O_3$ was chosen for this precursor study. Experimental parameters not only included the study of different precursor chemistries, but also the exploration of heating rate, treatment temperatures, and atmosphere. As it will be shown below, all three chemical routes would produce either Pb or PbO during pyrolysis, but both of these unwanted phases could be avoided with a special heating procedure for one of the three precursor chemistries.

2. Experimental

Three chemical precursor routes were employed to prepare $Pb(Zr_{0.5}Ti_{0.5})O_3$ powders: 1) one based on mixing hexanoates (long-chain, metal-organic molecules), 2) a second based on acetate complexing of alkoxides and 3) a third based on Ti- and Zr-alkoxide reaction with Pb-acetate. All chemistries produced a $Pb(Zr_{0.5}Ti_{0.5})O_3$ perovskite powder at higher temperatures.

The first method simply involved dissolving and mixing lead(II) 2-ethylhexanoate, zirconium 2-ethylhexanoate, and titanium 2-ethylhexanoxide in toluene; all 2-ethylhexanoates were obtained as commercial liquids. Each was assayed to determine their oxide yield to ensure its correct proportion to produce (50/50)PZT. The solution was left out in air overnight to allow evaporation of excess solvent, resulting in a very viscous solution which was subsequently heat treated for pyrolysis and crystallization observations.

The second precursor route was the acetic acid modifier process outlined by Schwartz et al.[6] Their method involves the addition of acetic acid to a titanium isopropoxide and zirconium butoxide solution in order to promote ligand exchange of all isopropanol and butanol groups. Following the addition of methanol, lead(IV) acetate was dissolved by refluxing at 75°C for 25 min. After the solution cooled, acetic acid, methanol, and water were added to the stock solution. A

precursor powder was prepared from the solution by vacuum distillation at room temperature. The resulting precursor powder was used to explore different pyrolysis and crystallization treatments.

The third precursor route studied was based on the reaction of Pb-acetate with Ti- and Zr-alkoxides introduced by Blum and Gurkovich, [4] and extensively studied by Budd et al. [5] Lead(II) acetate trihydrate was vacuum dehydrated at 100°C for 30 min. inside a 3-neck distillation flask. The flask was taken to a dry glove box, where ethanol, zirconium butoxide, and titanium isopropoxide were added sequentially, to produce an alkoxide concentration of 0.085 moles/liter of ethanol. The mixture was then refluxed at 85°C for 20 h to promote dissolution and reaction of the lead acetate. Upon cooling, the solution was hydrolyzed with an equal volume of deionized water by rapidly mixing the water into the solution. This immediately produced a gel-like solid, which was immediately placed in a drying oven at 90°C. The resulting precursor powder was used for pyrolysis and crystallization experiments.

The soap-like hexanoate precursor and the precursor powders from the acetic acid modifier and alkoxide processes were heat treated by directly inserting them into a preheated tube furnace, a process called "upquenching". Small Pt crucibles were used for the precursor powders and an alumina boat used for the viscous hexanoate precursor. Treatment temperatures ranged from 300°C to 700°C; both air and O_2 atmospheres were used. After upquenching, treatment periods ranged from 5 min to 1 h. Some powders were subjected to an initial low temperature pyrolysis step prior to heat treatment at higher temperatures. During this pyrolysis treatment, powders were held at 300°C up to 1 hour in either air or O_2. Following every heat treatment, the phase(s) within the powders were examined by x-ray diffraction (Sintag XRD 2000) with continuous scans between the angles of 10° and 70° 2Θ at 0.75°/min.

TGA (Dupont 951) was used to monitor the decomposition of the various precursors. The same powders-- from the alkoxide-based and acetic acid modifier processes-- and solution-- from the hexanoates-- used in the upquenching runs were characterized in the TGA. All weight loss data were collected at 10°C/min in a 50ml/min flow of air.

3. Results
3.1 Hexanoates
XRD data from specimens upquenched in air at 400°C with a 10 min hold and 500°C/5 min, 600°C/5 min, and 700°C°C/5 min are shown in Fig. 1. Partitioning of elemental Pb is evident by observed Pb and/or PbO XRD peaks in the 400 °C, 500 °C, and 600 °C patterns. After a 10 min treatment at 400°C, elemental Pb, t-PbO, and some o-PbO are observed (Fig. 1a). Similarly in Figure 1b (500°C/5 min), both elemental lead and lead oxide are observed, but with o-PbO as the chief PbO component, consistent with the phase diagram and the higher treatment temperature. In Figure 1c (600°C/5 min), no Pb is detected and only a trace of t-PbO is observed, while pyrochlore (or fluorite) and perovskite were the major phases in the powder. After 5 min at 700°C (Fig. 1d) all trace of PbO is gone and the pyrochlore (or fluorite) $\Rightarrow$ perovskite transformation nears completion.

Figure 2 shows similar partitioning of powders previously pyrolyzed at 300°C. One pattern in Fig. 2 was obtained from a powder prepared by firing the precursor solution in air at 300°C/30 min. This produced a sticky, brown, amorphous powder. When the powder previously pyrolyzed at 300°C/30 min was subsequently upquenched in O_2 at 400°C/5 min both Pb and PbO are detected, as shown by pattern (b).

Besides not being an appropriate precursor because it produces elemental Pb and PbO, it should also be noted that none of the hexanoate compositions could be upquenched in O_2. The reason for this is that, as observed during TGA experiments, these carbon-rich precursors combust in O_2 resulted in temperature spikes up to 200°C. Such self-heating limits the usefulness of upquenching and makes the thermal treatment condition unknown.

When Pb-hexanoate was pyrolyzed separately at 500°C/5 min, small, gray, spherical beads were observed with the optical microscope. XRD of the sample revealed that both t-PbO and Pb were present (Pb melts at 328°C).

3.2 Acetic Acid Modifier

Figure 3 shows XRD data taken from powders upquenched at (a) 300°C/5 min in air, (b) 400°C/5 min in air, and (c) 400°C/5 min in O_2. The powder was amorphous after the 300°C treatment and black. Elemental Pb partitioned during the the 400°C treatment in air. Pattern c, Fig. 3, shows that the Pb oxidizes to tetragonal PbO when pyrolyzed in O_2 instead of air. Pb and PbO free $Pb(Ti,Zr)O_3$ with the perovskite structure was obtained after heat treatment at higher temperatures (not shown in Fig. 3). When the powder was first treated with a low temperature pyrolysis step at 300°C for 20 min, Pb had partitioned out, as detected with XRD.

3.3 Alkoxides

Figure 4 shows the XRD data for alkoxide-derived powders upquenched at (a) 300°C/1 h in air, (b) 400°C/5 min in air, and (c) 400°C/5 min in O_2. As with the previous precursor chemistries, partitioning of lead has occurred. That is, an upquench at 400°C in air produces elemental Pb and some t-PbO, whereas the same upquench in O_2 produces mostly t-PbO with minor amounts of elemental Pb.

Formation of Pb (or PbO) could be avoided with the alkoxide chemistry when the precursor powder was first pyrolyzed in air at 300°C for 1hour. (This did not work with the two other precursor routes). Pattern (a) in Fig. 5 shows that the heat treatment in air at 300°C/1 h produces an amorphous material. Pattern (b) shows that the pre-pyrolyzed powder remains amorphous after it is upquenched to 400°C for 30 min. A crystalline phase is first detected only after the pre-pyrolyzed powder is treated in O_2 at 500°C/5 min. In Figure 5c two broad humps are evident and are attributable to an intermediate pyrochlore (or fluorite) [10] phase. This crystallization appears to have occurred without partitioning of any lead compounds. The final pattern in Figure 5 shows the onset of the pyrochlore (or fluorite) $\Rightarrow$ perovskite transition. The transformation is complete with only the perovskite remaining when the precursor is heated higher temperatures and/or longer treatment periods.

Another observation concerning the pyrolysis condition was color changes. The initial hydrolyzed alkoxide precursor powders were white. After 30 min at 300°C, the powders became black suggesting the presence of carbonaceous material.

After 1h at 300°C, the powders were yellow, the same color of the perovskite phase following full conversion to PZT at higher temperatures.

3.4 TGA Results

Figure 6 shows the TGA profiles from the (a) hexanoates solution, (b) acetic acid modified powder, (c) alkoxide-derived powder, and (d) alkoxide-derived powder after partial pyrolysis at 300°C for 1 hour. The curves attest to the increasing organic component of the precursors from the hexanoates to the acetic acid modified alkoxides to the alkoxides. The measured weight percent retained as oxide for the three precursor routes was 31, 61, and 83%, respectively. The partially pyrolyzed alkoxide-based powder retained 92% of its weight as oxide, a considerable increase from that of the untreated alkoxide-derived powder.

4. Discussion

Partitioning of elemental Pb and/or PbO during pyrolysis was observed for the three precursor routes investigated. Similarly, evidence of elemental Pb was found by Li et al.[11] in their XRD of $Pb(Zr_{0.8}Ti_{0.2})O_3$ powders heat treated at 400°C for 2h and, albeit unnoted, by Budd et al.[5] in their XRD study of $PbZrO_3$ powders. Both of these researchers used an alkoxide-based precursor procedure similar to the third process in this study. The partitioning of Pb and/or PbO during pyrolysis is consistent with the possible formation of elemental Pb at moderate oxygen partial pressures,[9] and the obvious presence of carbonaceous matter in all three chemical routes that could provide a local, low oxygen partial pressure during pyrolysis. The greater amount of PbO relative to elemental Pb observed during pyrolysis in oxygen relative to air suggests that elemental Pb is formed first and then oxidizes to PbO as the concentration of hydrocarbons diminish as more of the precursor is converted to PZT. It should be noted, that despite the formation of Pb (and PbO) during pyrolysis, $Pb(Zr_{0.5}Ti_{0.5})O_3$ could always be synthesized in short periods with the perovskite structure at temperatures $\geq$ 700 °C.

Crystallization of $Pb(Zr_{0.5}Ti_{0.5})O_3$, without the initial partitioning of Pb (or PbO) was exclusively achieved with the mixed alkoxide-based route only after a low temperature pyrolysis treatment was included in the procedure. This observation suggests that an oxygen partial pressure insufficient to cause the formation of elemental Pb could be achieved when the pyrolysis was performed at a lower temperature. Further, it suggests that the *rate* of hydrocarbon evolution during pyrolysis, which controls the local oxygen partial pressure, is important and must be controlled. Since this observation was exclusive to the chemical route that produced an apparent mixed alkoxide, the need to have Pb bonded to oxygen, as -Pb-O-(Ti, Zr)-O-, within the precursor appears important. In addition, TGA data in Fig. 6 shows that the mixed alkoxide precursor contains much less carbonaceous material relative to the other precursors. Thus, although the bonding of Pb with oxygen within the precursor at first appears important, the real reason why the mixed alkoxide route is more effective may simply be due to its lower content of carbonaceous material.

On-the-other-hand, heterogeneities have been shown to exist within alkoxide precursor solutions themselves. Ma and Payne[12] and Chae et al.[13] have isolated oligomers with stoichiometry ratios of 1:2 for Pb:Ti and Pb:Zr, respectively. This

indicates that at least at the atomistic level the solution is not homogenous. This also suggests that the remaining, unreacted Pb precursor (50% of the total for PZT compositions) may be free to form isolated Pb-rich pockets, further increasing the likeliness of producing partitioned crystalline Pb or PbO phases. This mechanism alone does not seem sufficient to produce the degree of PbO partitioning observed in this study. Any heterogeneities within the alkoxide-derived powder were not large enough to prevent the partitionless crystallization observed during pyrolysis treatment at 300°C.

The formation of Pb during the pyrolysis of precursors is not only important to our diffusion limited crystallization experiments, which are already underway, but also of significant to other precursor applications. For example, Chen and Chen,[14] using hexanoates and neodecanoates precursors to form PZT thin films on Pt coated Si, observed the formation of an unwanted, transient $Pt_{5+x}Pb$ intermetallic phase.

5. Conclusions

Pyrolysis conditions were shown to be important to control the production of homogeneous, amorphous $Pb(Zr_{0.5}Ti_{0.5})O_3$ powders synthesis from metal-organic precursors. Heat treatment in both air and O_2 resulted in the partitioning of Pb and PbO for the three precursor chemistries investigated. Formation of Pb (and PbO) could be avoided by first heat treating hydrolyzed, mixed alkoxide precursor powders at 300°C for 1hour. It is concluded that both the carbonaceous content of the precursor (lowest for the hydrolyzed, mixed alkoxides) and the rate of hydrocarbon release during pyrolysis is critical to avoid the formation of elemental Pb during pyrolysis.

References

1. C.D.E. Lakeman and D.A. Payne, "Processing Effects in the Sol-Gel Preparation of PZT Dried Gels, Powders, and Ferroelectric Thin Layers", J. Am. Ceram. Soc., 75 [11] 3091-6 (1992).

2. R.A. Assink and R.W. Schwartz, "^{1}H and ^{13}C NMR Investigations of $Pb(Zr,Ti)O_3$ Thin-Film Precursor Solutions", Chem. Mater., 5 511-7 (1993).

3. B.A. Tuttle, J.A. Voigt, D.C. Goodnow, D.L. Lamppa, T.J. Headley, M.O. Eatough, G. Zender, R.D. Nasby, and S.M. Rodgers, "Highly Oriented, Chemically Prepared $Pb(Zr,Ti)O_3$ Thin Films", J. Am. Ceram. Soc., 76 [6] 1537-44 (1993).

4. J.B. Blum and S.R. Gurkovich, "Sol-Gel derived $PbTiO_3$," J. Mater. Sci, 20, 4479 (1985).

5. K.D. Budd, S.K. Dey, and D.A. Payne, "Sol-Gel Processing of $PbTiO_3$, $PbZrO_3$, PZT, and PLZT Thin Films", Br. Ceram. Proc., 36 107-21 (1985).

6. R.W. Schwartz, R.A. Assink, and T.J. Headley, "Sectroscopic and Microstructural Characterization of Solution Chemistry Effects in PZT Thin Film Processing" in Ferroelectric Thin Films II Syposium, edited by A.I. Kingon, E.R.Myers, and B.A. Tuttle, (Mat. Res. Soc. Symp. Proc., vol. 243, Pittsburgh, 1992), pp. 345-54.

7. G. Yi, Z. Wu, and M. Sayer, "Preparation of $Pb(Zr,Ti)O_3$ Thin Films by Sol-Gel Processing: Electrical, Optical, and electro-optic Properties", J. Appl. Phys., 75 [5] 2717-24 (1988).

8. R.W. Vest and W. Zhu, "Films of 60/40 PZT by the MOD Process for Memory Applications", Ferroelectrics, 119 61-75 (1991).

9. J.V. Mantese, A.L. Micheli, A.H. Hamdi, and R.W. West, "Metalorganic Deposition (MOD): A Nonvacuum, Spin-on, Liquid-Based, Thin Film Method," MRS Bul. 14 [10] 48-53 (1989).

10. A.P. Wilkinson. J.S. Speck, and A.K. Cheetham, "In Situ X-ray Diffraction Study of Crystallization Kinetics in $PbZr_{1-x}Ti_xO3$ (PZT, x=0.0, 0.55, 1.0)," Chem. Mater., 6 750-4 (1994).

11. S.Li, R.A. Condrate, and R.M. Spriggs, "The FTIR and Raman Spectra of Lead Zirconate Titanates (PZT) Prepared by a Sol-Gel Process," J. Canadian Cer. Soc., 57 61-5 (1988).

12. L. Ma and D.A. Payne, "Studies on the Nature of a Lead Zirconate Titanate (PZT) Precursor Solution. Isolation and Structural Characterization of $[PbZr_2(O)(OOCCH_3)_2(OCH_2CH_3)_6]_2$," Chem. Mater., 6 875-7 (1994).

13. H.K. Chae, D.A. Payne, Z. Xu, and L. Ma, "Molecular Structure of a New Lead Titanium Bimetallic Alkoxide Complex, $[PbTi_2(\mu_4-O)(OOCCH_3)(OCH_2CH_3)_7]_2$: Evolution of Structure on Heat Treatment and the Formation of Thin-Layer Dielectrics," Chem. Mater., 6 1589-92 (1994).

14. S.-Y. Chen and I.-W. Chen, "Temperature-Time Texture Transition of $Pb(Zr,Ti)O_3$ Thin Films: I, Role of Pb-rich Intermediate Phases", J. Am. Cer. Soc., 77 [9] 2332-6 (1992).
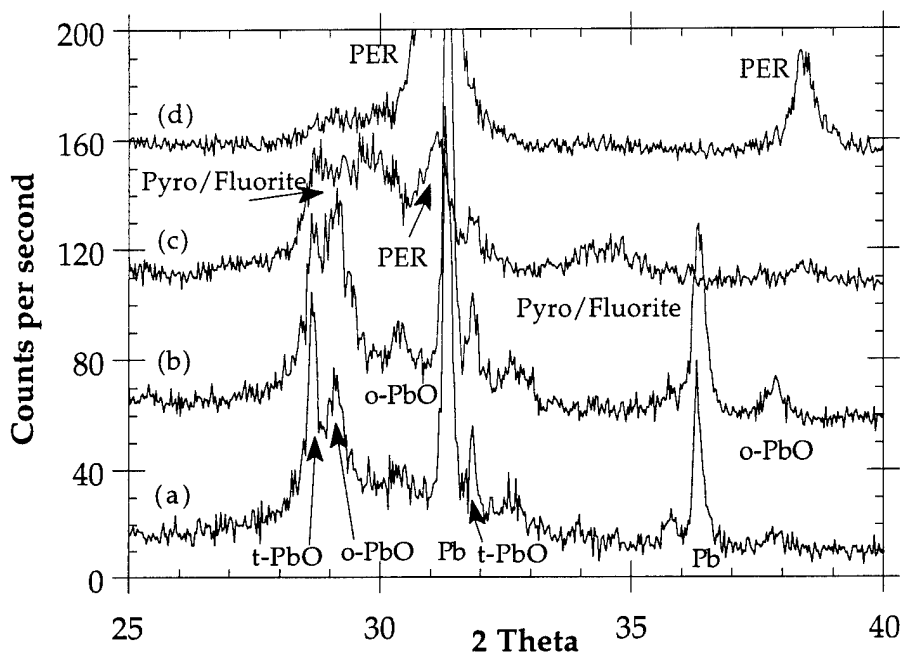
Figure 1.   XRD patterns from hexanoate-derived powders upquenched at (a) 400°C for 10 minutes, and (b) 500°C, (c) 600°C, and (d) 700°C for 5 minutes in air.
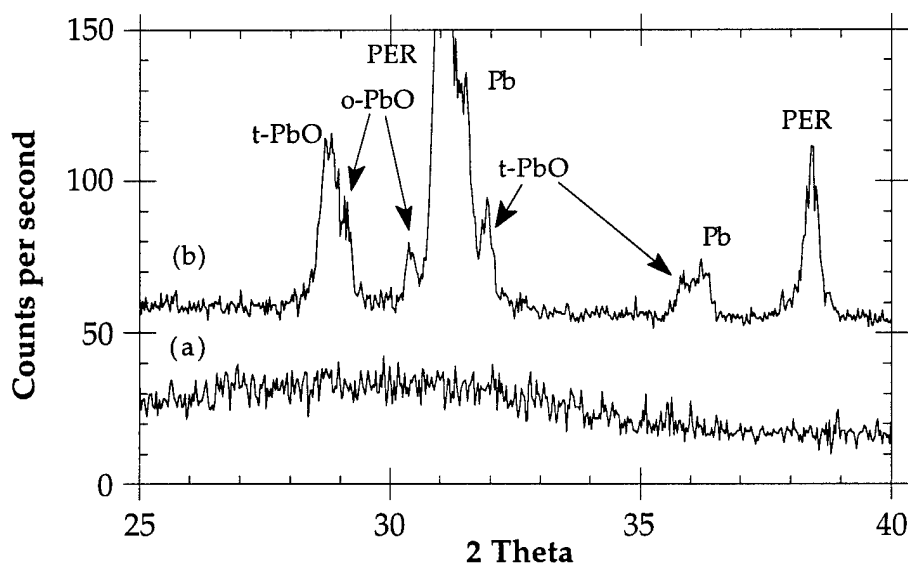

Figure 2.   XRD data from hexanoate-derived powders (a) fired at 300°C for 30 minutes in air and (b) sequentially upquenched at 400°C for 5 mintes in O_2.
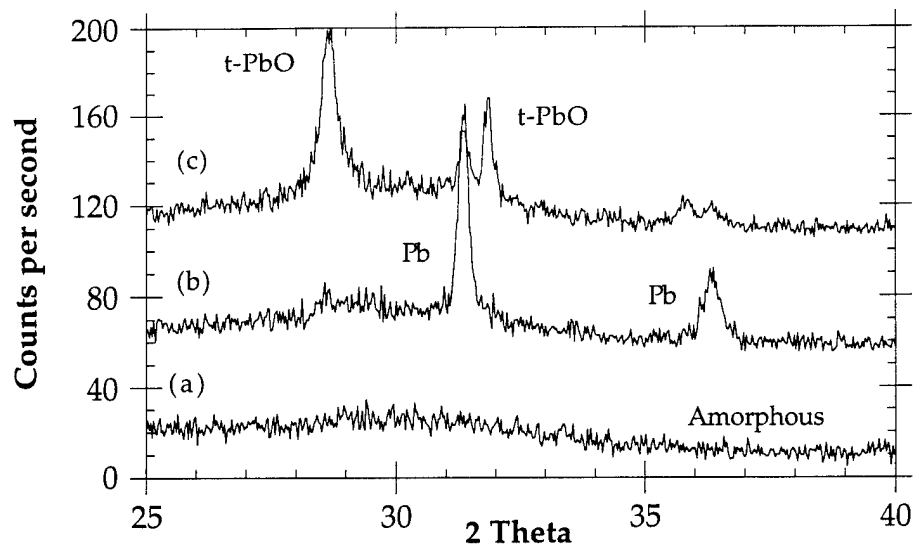
Figure 3.   XRD patterns from powders prepared with the acetated complexed percursors upquenched at (a) 300°C and (b) 400°C for 5 minutes in air, and (c) 400°C for 5 minutes in O_2.
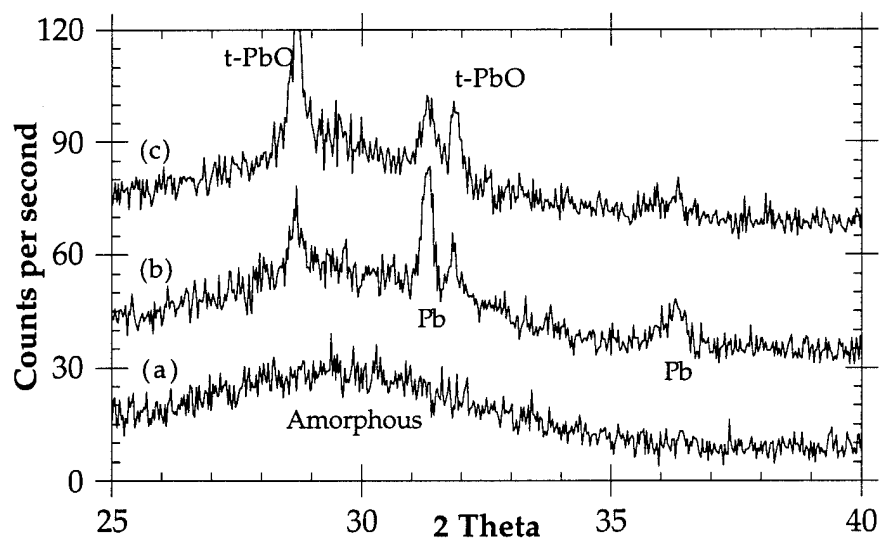

Figure 4.   XRD data from mixed alkoxide-derived powders upquenched at (a) 300°C for 1 hour and (b) 400°C for 5 minutes in air, and (c) 400°C for 5 minutes in O_2.
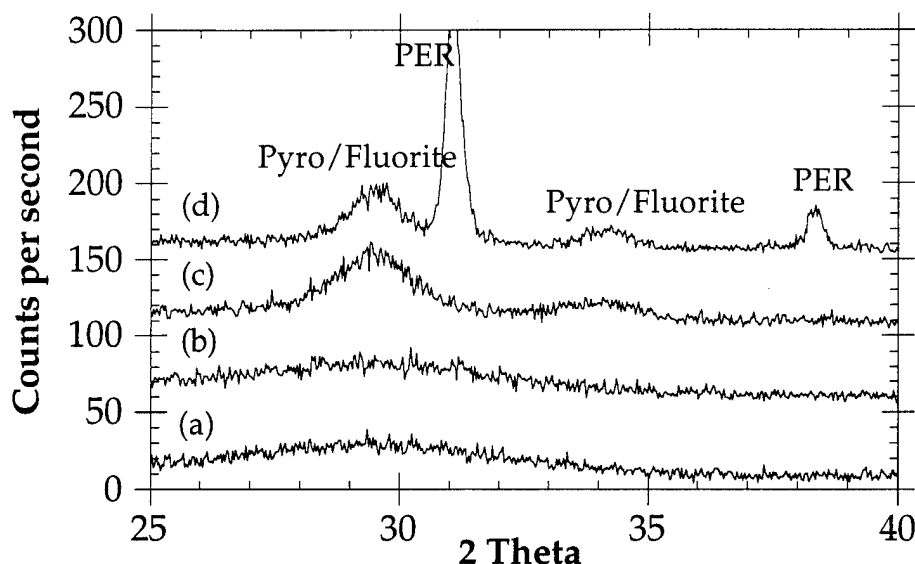
Figure 5. XRD patterns from mixed alkoxide-derived powders preveously put through 300°C pyrolysis treatment for 1hour in air. The powder in (a) was pyrolzed without further heat treatment. The remaining patterns were collected from powders subsequently upquenched at (b) 400°C for 30 minutes and (c) 500°C and (d) 600°C for 5 minutes in O_2.
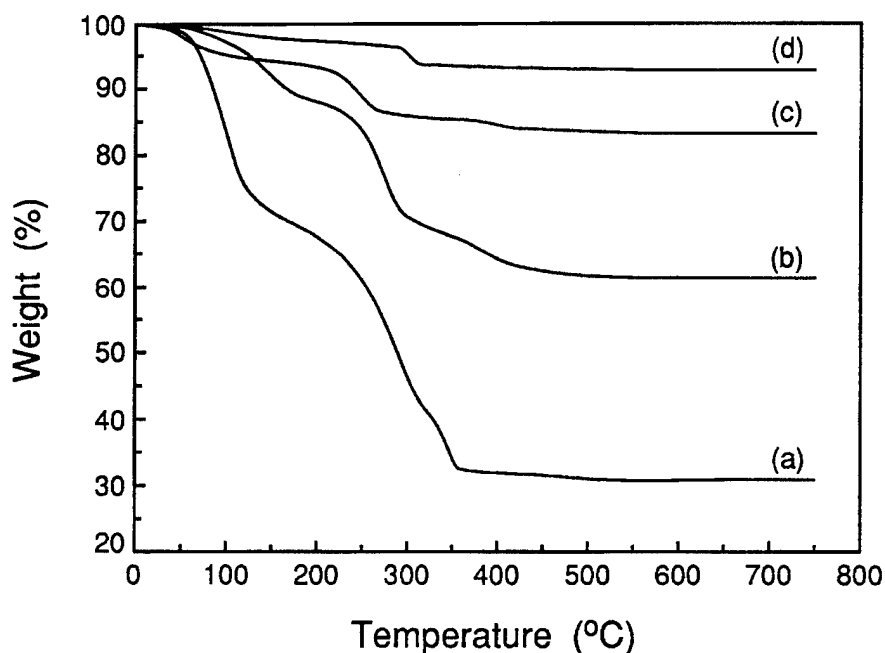

Figure 6. TGA profiles collected from (a) hexanoates, (b) acetic acid modified alkoxides powders, (c) alkoxide-derived powders, and (d) alkoxide-derived powders previously put through 300°C pyrolysis treatment for 1hour in air.